The earthquake sedimentary record in the Western part of the Sea of Marmara, Turkey

L.Drab, A.Hubert-Ferrari, S.Schmidt, P.Martinez

Abstract

The submarine part of the North Anatolian Fault (NAF) is a very significant hazard for the 12 million people living in Istanbul (Turkey). An accurate seismic risk assessment necessitates paleoseismological data, which can be retrieved in the Marmara Sea by using sedimentary cores. Here a record of turbidites was obtained in five cores spanning the Tekirdağ Basin, the Western High and the Central Basin linked by the Tekirdağ Fault Segment. The turbidites are synchronous at different sites across the two basins and through the structural high pointing to shaking by earthquakes as a triggering mechanism. In particular the M=7.4 1912 Mürefte earthquake left a distinctive sedimentary imprint in all the studied cores. Radiocarbon dating implies a turbidite recurrence interval of about 300 years. The low number of seismoturbidites documented in the Central Basin compare to the Tekirdağ Basin suggests quasi-synchronous ruptures of the Tekirdağ Segment and the adjacent Central Segment of the NAF or a partial seismic slip on the Central Segment. Both scenarios have implications regarding seismic hazard. Finally though we obtained a paleoseismological record of the ruptures along the Tekirdağ Segment, further chronological constraints are needed to better date the events and to confirm the completeness of the obtained record.

Introduction

Hazard risk assessment for populations living in tectonically active areas can be improved using paleoseismology, by building an extended database of major earthquakes and earthquake recurrence time (Fraser et al., 2010). Even though most studies in this field of inquiry were historically based on on-land field work, e.g. in California, in Turkey, in Italy, in Himalayas, in Tibet (Dolan et al., 2003; Weldon et al., 2004; Galli et al., 2008; Kondo et al., 2008; Fraser et al., 2010; Klinger et al., 2011), recently interesting offshore studies appeared (Goldfinger et al., 2003a; Goldfinger, 2011). These studies use the identification of mass-wasting deposits triggered by large earthquakes to obtain records of events over 1000s of years (McHugh et al., 2006; Beck et al., 2007). Mass-wasting deposits related to earthquakes have a specific signature and can be distinguished from other deposits emplaced by hyperpycnal flow, wave storm loading among others (Gorsline et al., 2000; Nakajima and Kanai, 2000; Shiki et al., 2000; Beck et al., 2007). Earthquake triggered turbidites may mobilise 5 to 10 times the sediment volume of classical turbidites (Gorsline et al., 2000) and usually show liquefaction or flaser bedding structures (Beck et al., 2007). Their granulometric signature reflects a high energy transportation mechanism forming a mass flow and a very large suspension cloud (Shiki et al., 2000). As a result seismoturbidites have a sharp and wavy erosional base (Shiki et al., 2000), and can be divided into a basal sand sublayer and a thick silt sublayer characterized by a poor size grading and coeval deposition of sand, silt and clay particles (Nakajima and Kanai, 2000; Shiki et al., 2000).

In this paper, we study the turbiditic sedimentation in the Marmara Sea, which is crossed by the North Anatolian Fault, a major active strike-slip fault rupturing in M$\geq$7 earthquakes. The presence of the urban area of Istanbul on its shoulder, where about 12 M people live, makes this region a major spot for seismic hazard studies. We identified turbiditic deposits in five 3 to 4 m long cores which sample its different basins and highs. We then use global sedimentological changes to correlate the different cores and to characterize the general depositional pattern in the Marmara Sea. Radiogenic lead data allow us to discriminate the turbidites triggered by the 1912 earthquake. The granulometric characteristics of the other turbidites, their lateral extent and the synchronicity of proximal and distal deposits are used to infer a seismic trigger. Finally, we discuss the paleoseismological implication of the identified seismoturbidites.

1 Settings

1.1 Tectonic setting

The North Anatolian Fault (NAF) is a 1500 km long dextral strike slip fault accommodating the westward extrusion of the Anatolian Plate (Barka and Kadinsky-Cade, 1988; Sengör et al., 2005). In the Marmara Sea area, the NAF separates into branches spreading out the deformation over a width of 130 km (Barka and Kadinsky-Cade, 1988). The northern branch of the NAF accommodates most of the deformation (McClusky et al., 2003) and runs across the 170 km long Marmara Sea.

The Marmara Sea is composed of three aligned marine pull apart basins reaching a maximum water depth of 1250 m (Le Pichon et al., 2001; Armijo et al., 2002; Sarı and Çağatay, 2006). From West to East the basins are called Tekirdağ, Central and Çınarcık. They are respectively associated with the present active Tekirdağ, Central and Çınarcık Fault Segments (Fig. 1). The different faults segments and the related basins have been imaged by seismic reflection and refraction profiles (Seeber et al., 2006; Carton et al., 2007; Bécel et al., 2009) and modelled (Hubert-Ferrari et al., 2000; Muller and Aydin, 2005). The basins are separated by two topographic ridges: the Western High and Central High with a respective water depth of 700 m and 900 m (Le Pichon et al., 2001; Armijo et al., 2005). The basins are sensitive to mass-wasting events triggered by major earthquakes rupturing the fault strand, which crosses them (McHugh et al., 2006; Sarı and Çağatay, 2006; Beck et al., 2007).

1.2 The historical earthquake record

The northern branch of the NAF in the Marmara Sea is a major active fault characterized by a GPS based right-lateral slip rate about 20 mm/yr (McClusky et al., 2003). The resulting accumulated stresses are episodically released by major and destructive earthquakes recorded in history over 2000 years (Ambraseys, 2002). During the 20^{th} century, the 1912 M = 7.4 Mürefte earthquake ruptured the Ganos Segment located West of the Marmara Sea and probably also the offshore part of the Tekirdağ Segment (Armijo et al., 2005; Aksoy et al., 2010). In 1999, the M= 7.4 Izmit earthquake took place just east of the Marmara Sea (Hubert-Ferrari et al., 2000). Five other events with M>7 occurred during the period from 1509 to 1900 (1719, 1754, 1766 May, 1766 August, 1894) (Fig. 1, Ambraseys 2002; Pondard et al. 2007). The historical record provides earthquake damage data restricted to the onland borders of the Marmara Sea and cannot be used alone to determine the epicenters and surface ruptures. Even recent earthquakes database do not provide routinely accurate earthquake epicenters and foci locations (Örgülü, 2011). Finally, submarine scarps associated with past recent ruptures in 1912 and possibly in 1894 complement the seismological data set (Armijo et al., 2005; Pondard, 2006).

1.3 Previous sedimentological core studies in the Marmara Sea

The Marmara Sea connects the Black Sea to the Aegean Sea through the Bosphorus and Dardanelles straits. Because of its particular geographic situation, it is highly sensitive to climatic and environmental changes and was the focus of multiple sedimentological investigations (Çağatay et al., 2000; Abrajano et al., 2002; Hiscott et al., 2002; Major et al., 2002; Mudie et al., 2002; Vidal et al., 2010). A key issue for these studies is the understanding of the nature of the reconnection between the Black Sea and the Mediterranean Sea (catastrophic Major et al. 2002; or progressive Çağatay et al. 2000; Hiscott et al. 2002) $\sim$ 9 kyr BP ago (Çağatay et al., 2000; Vidal et al., 2010).

Recent environmental changes related to anthropogenic disturbances were also identified. In particular, pollen studies (Mudie et al., 2002) put forward the occurrence of a progressive deforestation starting 4 kyr ago in the watershed surrounding the Marmara Sea. During the Beyşehir Occupation Phase (ca. 1300 years BC to ca. AD 200–800 years; Eastwood et al. 1998) vegetation changes and land degradation have been documented in the Lakes Manyas and Ulabat (Kazanci et al., 2004). In both lakes, which are part of the Kocasu River, a major source of sediments for the Marmara Sea, higher rates of sedimentation started around 2 kyr BP. In parallel a progressive increase in sedimentation rate on the Marmara Southern Shelf occurred (Kazanci et al., 2004) at the same time as the formation of the most recent sapropel, 4750-3500 14C years BP ago (Çağatay et al., 2000). Eris et al. (2007) also suggested that the growth of the prodelta at the entrance of the Bosphorus was related to an increase in sediment supply triggered by the clearing of forests in watersheds.

In addition to paleoclimatic investigations, paleoseismologic studies have recently used turbidites for deciphering the earthquake history (McHugh et al., 2006; Sarı and Çağatay, 2006; Beck et al., 2007). Multi-proxy analyses were performed on cores coming from Central Basin (McHugh et al., 2006; Beck et al., 2007) and Tekirdağ Basin (McHugh et al., 2006). Both authors conclude that: (1) significant turbiditic deposition directly related to earthquake shaking occurs in the Marmara Basin (McHugh et al., 2006; Beck et al., 2007), (2) basins' filling is mainly controlled by active faults (Uçarkuş, 2010) and may document earthquake rupture along the associated fault segments (McHugh et al., 2006; Beck et al., 2007), (3) seismoturbidites are associated with oscillating bottom currents (seiche) with variable suspended load or bedload (Beck et al., 2007).

2 Material

The cores studied (Klg02 to Klg08) were collected in the Marmara Sea during the Marmascarps mission in 2002 shortly after the 1999 M=7.4 Izmit earthquake (Armijo et al., 2005). The coring sites are similar to locations of ROV short cores (Uçarkuş, 2010) and long cores studied in Beck et al. (2007), Londeix et al. (2009), Vidal et al. (2010). The seven Kullenberg cores are 3.5 m to 4.5 m long (Table 1) and are distributed in specific areas along the fault (Fig. 1). They provide a link between very short interface cores (ROV) and the very long cores of the Marion Dufresne Cruise in which upper meters are often missing or strongly disturbed.

The Klg05 and Klg08 cores are situated 6 km apart in the southern part of the Tekirdağ Basin, along the Tekirdağ Segment of the NAF, at the outlet of deep canyons (Fig. 1). Further east the Klg06 core samples the intersection between the Western High and the Tekirdağ Basin, and the Klg07 core samples the intersection between the Central Basin and the Western High. These two cores lying 15 km apart are close to the Tekirdağ Segment. Klg02 is located in the inner part of the Central Basin pull apart (Armijo et al., 1999) between the Tekirdağ and the Central Segments of the NAF. Klg03 and Klg04 sample the Çınarcık Basin. The paper focuses on the Klg02, Klg05, Klg06, Klg07 and Klg08 cores, but the XRF-data obtained for the Klg04 core is presented here because it highlights global sedimentary changes occurring across the whole Marmara Sea.

3 Methods

Core processing, imaging and physical properties The sedimentary facies observed in cores were described first to provide a basic core log. The visual core description was based on colour, bedding, sedimentary structures and disturbances, grain size distribution, texture, bioturbation and fossil content. This description was refined by using X-ray radiograms, granulometric data, magnetic susceptibility measurements and XRF-scanning data.

In the X-ray pictures (EPOC scopix system in Bordeaux 1 University), the grey scale is proportional to the X-ray penetration into the core and to the sediment density, with sand being usually black and clay light grey (Migeon et al., 1999). The X-ray imagery was particularly useful to identify all possible sedimentary structures like laminated coarser episodes, low angle symmetric cross lamination, ball-and-pillow structures, water-escape structures, displacements previously interpreted in sedimentary cores sampling the Tekirdağ Basin as specific imprints of major earthquakes by Beck et al. (2007).

The magnetic susceptibility measurements were performed on the split cores using a bartington MS2E sensor with 5 mm interval at room-temperature. The data provide a first-order identification of layers enriched in coarse detrital material (Fe, Mg, Ti) which can characterize the base of turbidites (Butler, 1992; Tauxe, 2010). Microgranulometric analyses were performed on bulk sediment sub-samples from u-channels at 10 mm intervals using a Malvern mastersizer 2000s. Percentage of clay, silt and sand particles were computed as well as mode, median, mean, skewness and kurtosis indices (Folk, 1968). The data help to characterize turbidites in term of depositional process (Pettijohn et al., 1987; Sperazza et al., 2004).

XRF XRF data collected by X-ray fluorescence on an Avaatech XRF core scanner were used to correlate cores between the basins and the Western High and to refine sedimentological and geochemical processes associated with turbiditic deposition. The split-core sections were measured every 5mm with energies of fluorescence radiation of 10 keV and 30 keV to reach a large spectra of elements comprising Al, Si, S, Cl, K, Ca, Ti, Mn, Fe, Br, Pb, Rb, Sr, Zr. The elemental distributions initially expressed in counts per second, were standardized to get a better comparison of the variations of intensity through the different cores. As intensities are only a semi-quantitative measurement of the real elemental composition, we used ratios that provide the most easily interpretable signal of relative changes in chemical composition, and minimize the risk of drawing erroneous conclusions from XRF data (Palike et al., 2001; Vlag et al., 2004; Bahr et al., 2005). The Ca/Ti ratio was exploited because it represents autochthonous productivity in the Sea (Ca) with respect to terrigenous allochthonous input (Ti), and because it is considered as a reliable proxy in the nearby Black Sea environment (Bahr et al., 2005).

Age dating AMS ^{14}C dating was performed on foraminifers (planktonic and benthic), bulk sediment and on shells in AEON laboratories and ARTEMIS LMC14 laboratory in the LSCE, Orsay.
Sediment accumulation rate for the last century was derived from profiles of excess ^{210}Pb activity ($^{210}Pb_{xs}$). ^{210}Pb and ^{226}Ra activities were measured using a semi-planar γ detector at EPOC in the University of Bordeaux 1 (Schmidt et al., 2009). Activities are expressed in $mBq.g^{-1}$ and errors are based on 1 standard deviation counting statistics. Excess ^{210}Pb was calculated by subtracting the activity supported by its parent isotope, ^{226}Ra, from the total ^{210}Pb activity in the sediment. Errors in $^{210}Pb_{xs}$ were calculated by propagation of errors in the corresponding pair (^{210}Pb and ^{226}Ra). The sedimentation rates were calculated from $^{210}Pb_{xs}$ profiles using the constant flux - constant sedimentation model (Robbins, 1978):

$$[^{210}Pb_{xs}]_z = [^{210}Pb_{xs}]_0 exp(-z\frac{\lambda}{S}) \quad (1)$$

where $[^{210}Pb_{xs}]_{0,z}$, are the activities of excess ^{210}Pb at surface, or the base of the mixed layer, and depth z, λ the decay constant of ^{210}Pb ($\lambda = 0.0311$ yr^{-1}), and S the sediment accumulation rate.

4 Results

4.1 Main features of sedimentation in the Marmara Sea

Visual inspection shows that all cores have a very uniform silty-clay lithology with few sandy laminations and rare gravelly layers containing numerous shells (indicated in red in the Figs. 4, 5, 6). The colour of the cores is predominantly olive green changing into dark grey with sandy laminations.
X-ray imagery shows a succession of dark sub-layers that are progressively grading to greyer colour (Fig. 3 event e6 in Klg05) and in places to light grey colours (Fig. 3 event 4 in Klg02) defining what

we call here a sedimentary event. The thickest dark layers correspond to sandy laminations and to gravelly layers identified during visual inspection. The dark grey, grey to light grey sequences show an important thickness range from 10 cm to more than 1 m thick. These sequences form about 80% of the sedimentary record of cores located in deep basins (Klg02, Klg05 and Klg08). X-ray pictures show detailed textural and structural changes in the three sublayers. Dark grey sublayers have a sharp basal surface (Fig. 2: 263 cm), which can be wavy indicating erosion (Figs. 2, 3) and associated with strong structural and cross disturbances (Figs. 2, 4). The overlying intermediate grey sublayer shows numerous thin parallel laminations in greater concentration near its base (Fig. 3 events e3 and e4 in Klg02 and e6 in Klg05) that can be link to oscillating currents (Beck et al., 2007). The sequence is capped by a light-grey sublayer with possible traces of bioturbation (Figs. 2, 3-Klg05). Similar events were already described in the Marmara Sea by using X-ray images, and were interpreted as the sedimentary rework of major earthquakes (McHugh et al., 2006; Beck et al., 2007).

Grain size measurements are similar for all cores with a dominance of silt-sized particles. Sieving shows that silt-sized particles are a mixture of mineral grains, different kind of shells including foraminifers, marine and terrestrial organic material among others. A systematic trend is observed in the upper part of cores characterized by a progressive increase in the percentage of silt-sized particles and a coeval decrease in the percentage of clay-sized particles (Fig. 2). All cores show multiple fine-grained sand deposits which systematically match with the dark sublayers identified in X-ray imagery and with high values in magnetic susceptibility, χ (Fig. 4, 5). In the overlying grey sublayer, silt usually reaches a maximum just above the sand layer and, slowly decreases upward to a minimum or stays nearly constant. The top light grey sublayer shows a relative increase in clay compared to silt. We thus interpret sedimentary events composed of (1) a basal sandy sublayer possibly erosive, (2) an intermediate laminated silt sublayer overlain by (3) an upper clayey silt sublayer with some bioturbation as major turbidites. We also identify in the cores very thin sand lamina that could correspond to minor turbidites. They typically have less than half of the volume of the smallest major turbidite identified in the same core.

To constrain the depositional pattern of the major turbidites, their textural characteristics are accessed by computing distribution parameters like mean, sorting, skewness, kurtosis (Folk 1968; Fig. 3 e6-Klg05 and e4-Klg02). Major sandy turbidites have the following characteristics. (1) the basal layer of the turbidites often shows multiple pulses, (2) grain size change between the sand and the silt sublayers is abrupt, (3) change in grain size, sorting and skewness can also be abrupt in the silt and clayey silt sublayers, whereas the decrease in kurtosis is generally gradual. The top clay-rich part of the turbidite is marked by a minima in sorting and a skewness around zero.

The major turbidites have also a distinct XRF signature. They typically show a local increase in zirconium (Zr) content (Figs. 2-b, 4). The sand sublayers are characterized by a decrease in bromine (Br) content whereas a relative increase in titanium (Ti) is observed in both the underlying sandy and silt-rich sublayers. Manganese (Mn) shows a sharp increase just below the basal sandy sublayer. The transition to the hemipelagic sedimentation is marked by a rising until a maximum in K, Ca or in Ca/Ti ratio. These elements do occur in proportion in the hemipelagic sedimentation (Fig. 8). Minor turbidites do not have a noteworthy XRF signature.

The stratigraphic logs of cores presented in Figs. 4, 5, 6 show the X-ray intensities, the magnetic susceptibility, the granulometric measurements and XRF data. The dark Zr enriched sand base, the laminated grey silt sublayer and the clayey silt top sublayers are shown with different grey scale colours, and labelled downward from the top of the core. Minor turbidites are not labelled.

4.2 Specific features of each site

In the Tekirdağ Basin, the 350 cm long sedimentary record of the core Klg05 (Fig. 4) shows ten major turbidites. Sedimentary events are characterized by (1) a sharp sand sublayer with χ and/or Zr peaks overlain by lamina, (2) an increase in Ti content in the basal and silt sublayers, (3) a Mn peak beneath the basal sand. Standing alone thin sandy layers are interpreted as minor turbidites. The largest turbidites labelled e5 and e6 at 160 cm and 233 cm depth have a gravelly base and a respective thickness of 55 cm and 70 cm (zoom pictures on Fig. 4). To assess the depositional pattern of these turbidites, distribution parameters (mean, sorting, skewness, kurtosis) are calculated and divided in layers labelled I, II, III and IV (Fig. 3). Above the gravelly base event e5 shows successively two sandy peaks, an inverse grading in the silty sublayer (mean size in phi decreases in Fig. 3) followed by an abrupt change in mean-sorting indexes then by normal grading. In event e6 the two basal sandy peaks (I in Fig. 3) are overlain by a first fining upward sublayer with gradually increasing sorting and decreasing skewness (layer II). Layer II is capped by additional sublayers with nearly constant mean, skewness and sorting separated by an abrupt change (III and IV in Fig. 3). In the sorting–skewness diagram, grain size evolves gradually towards smaller skewness and better sorting values, but with distinctive groups representing the different sublayers. The geochemical evolution of the two turbidites also show coeval changes with the granulometry (Fig. 3). K intensity shows a gradual evolution through the turbidite similar to the kurtosis index and might reflect a relative increase in illite in the grain assemblage. The characteristics of events 5 and 6, in particular non-gradual changes in grain size and the two coarser basal pulses, are representative of other major turbidites recorded Klg05.

In the inner part of the Central Basin, the core Klg02 shows eleven major turbidites (Fig. 5), which display a greater diversity regarding their geochemistry and textural patterns than in Klg05. The observed diversity may reflect a larger variability in the emplacement and in the sources of turbidites in the inner Central Basin compared to the Tekirdağ Basin. Our identification of major turbidites was based on disturbances identified in the X-Ray images combined with granulometric and geochemical data suggesting sudden detrital input. Like in Klg05 there are two large turbidites labelled e3 and e4 occurring at 150 cm and 205 cm depth with a respective thickness of 70 cm and 50 cm. The shallowest e3 turbidite presents a gravelly base associated with a strong χ peak (layer I in Fig. 3 and Fig. 5). The overlying deposit shows a gradual decrease in χ with two distinct phases. The silty sublayer (labelled II in Fig. 3) shows small variations in mean and in sorting without trend except at the boundary of the overlying clayey-silt sublayer characterized by step changes in all parameters. This top layer (III in Fig. 3) is characterized by increasing sorting and a constant mean grain-size. The other large event e4 has a sandy base with multiple laminations (I in Fig. 3) and a strong χ peak. The overlying layers II and III present an atypical very low χ with very little geochemical changes (see Fe/Ca in Fig. 3) and are similar to homogenites documented by Bertrand et al. (2008). Above the basal laminated layer kurtosis and mean do not change significantly whereas skewness and sorting have similar but very gradual evolutions. In the sorting–skewness diagram, the data is similar to the e6 turbidite in Klg05 with a gradual evolution toward better sorting values and smaller skewness except at the top.

In the Western High, the granulometric trends in Klg06 and Klg07 cores differ from the cores in the basins (Fig. 6). Sand size particles are less than 1% with few peaks. The major part of the signal comes from the silt-sized particles profile, which is between 94% and 90%. We focus on the top 80 cm of the cores in figure 6 but complete data are included in the Supplemental Data.

In Klg06 we identified eight silt turbidites in the X-ray imagery that correspond to a punctual upward increase in grain size capped by a relative increase in clay (Fig. 6). The layers are associated with manganese peaks, and an increase in Ti/Al ratio. The two thickest and most distinctive silt turbidites labelled e5 and e7 are recorded at depth of 58 cm and 85 cm. The e5 turbidite has the largest sand peak and e7 is associated with the only distinct magnetic susceptibility peak in the core. Both turbidites have a strong XRF signature characterized by an increase in the Ti/Al ratio in the main body and a marked increase in manganese content beneath.

In the core Klg07, ten fine grained turbidites were recognised. These turbidites are thin and are identified based on faint disturbances in the X-ray imagery, grain-size changes, χ peaks and geochemical spikes in Zr, Sr/Ca and Mn (Fig. 6). Four turbidites labelled e1, e5, e8 and e9 at 10 cm, 32 cm, 58 cm and 69 cm in depth have a sandy base. Events e5 and e8 correspond to the largest events and show zirconium, manganese and magnetic susceptibility peaks.

4.3 Age constraints

4.3.1 Excess $^{210}Pb_{xs}$ activities

The age of sediments in the first 20 to 50 cm of all cores was constrained by using unsupported lead data. Excess ^{210}Pb activities for each core are consistent with the activities of the nearby ROV cores recovered during the same cruise (Fig. 7). In the first 10 cm of cores Klg05, Klg08 and Klg06, $^{210}Pb_{xs}$ activities present an exponential decay with increasing depth with no evidence of reworking, as confirmed by X-ray imagery. The limited shift between ROV and Klg profiles indicates a moderate loss of surface sediment up to 6 cm for Klg08 during coring. The ^{210}Pb derived sedimentation rates are 0.23 cm.yr^{-1} for Tekirdağ Basin (Klg08 and Klg05), 0.12 cm.yr^{-1} for Western High (Klg06). These rates are interpreted to represent steady hemipelagic sedimentation rates.

The uppermost section of the cores Klg02 and Klg07 shows constant $^{210}Pb_{xs}$ activities in an inferred mixed layer. In core Klg02, the 35 cm thick mixed layer is identical to the ^{210}Pb trend in the nearby core C4 studied in McHugh et al. (2006) (Fig. 1) and is associated with two thin sandy turbidites visible in the X-ray imagery and in the granulometric data. We have no explanation for the origin of this mixed layer.

In core Klg07, the mixed layer is only 5 cm thick. In the nearby 20 cm long core collected using a ROV, there is no mixed layer that suggests that it is a coring artefact. Below the mixed layer, ^{210}Pb activity shows a rapid exponential decay with depth. The inferred background hemipelagic sedimentation rate is 0.15 cm.yr^{-1} in Klg02 (Central Basin) and is 0.10 cm.yr^{-1} in Klg07 (Western High) similar to the Klg06 rate.

4.3.2 Radiocarbon age dating

Radiocarbon age dating shows globally a large disparity depending on the material used (shells, bulk sediment and foraminifers) (Table 2). Ages calculated from shells in cores Klg05, Klg08 and Klg06 generally overestimate the expected age of the host sediment, and indicate significant reworking and external sedimentary supply from the shelf associated with turbiditic deposition. Ages of bulk sediments (TOC and TIC) are also too old and are not further discussed. Ages obtained from both planktonic and benthic foraminifers extracted on the top of turbiditic events are the most reliable and thus form the basis for our chronology.

Planktonic foraminifers were obtained in sufficient abundance to be dated only at a few locations, so benthic foraminifers were also dated. To further constrain our age model, we correlate our records with nearby published sedimentary cores. In the Western High, by comparing the Klg06 core to the core MD2430 studied by Vidal et al. (2010), the Younger Dryas transition would be below the core bottom which is in agreement with the obtained uncalibrated age of 6880 yr BP at the core bottom. The Klg07 core also in the Western High has magnetic susceptibility measurements similar to the core MD2430, and uncalibrated radiocarbon ages of 2500 yr BP at 61 cm depth, 4815 yr BP at 212 cm depth and 7875 yr BP at 297 cm depth compatible with the age model of the MD2430 core (Fig. 14 in the appendices; Vidal et al. 2010). The Klg05 and Klg02 cores in the basins can be correlated to the C4 and C8 cores of McHugh et al. (2006). In Klg05, the uncalibrated ages of 1090 yr BP at 48 cm depth, 1735 yr BP at 167 cm depth and 2185 yr BP at 250 cm depth agree with the 14C-age of 1320 yr BP at 55 cm depth and 1460 yr BP at 65 cm depth in core C4 (Fig. 15 in the appendices; McHugh et al. 2006). The Klg08 core has 14-C ages of 2880 yr BP at 73 cm depth, 4670 yr BP at 145 cm depth and 12770 yr BP at 335 cm depth (Fig. 11).

The longest records spanning 6000 to 12000 years are reached in the Western High, and on the uplifted side of the NAF in the Tekirdağ Basin. In the Tekirdağ and Central Basins, we have a sedimentary record lasting 3000 to 4000 years.

5 Interpretation

5.1 Variations in sedimentation pattern in the Marmara Sea

The correlation of the Klg02 to Klg08 cores across the whole Marmara Sea was done combining granulometry, Ca/Ti ratio, Ti, Pb, Br and Sr intensities with the obtained chronological data. Marked geochemical and granulometric variations are used as chronological markers and are tentatively interpreted as global changes in the sedimentation pattern of the Marmara Sea related to anthropogenic disturbances.

The cores Klg07 and Klg08 covering the longest time frame show similar Ca/Ti variations (Fig. 8-part a). Based on radiocarbon dating and χ measurements the Klg07 core can also be related to the core MD2430 studied in Vidal et al. (2010) (Fig. 14 in the appendices). The base of Klg07 is characterized by high χ and was deposited at the end of the glacial period (Fig. 14 in the appendices). Between 2 and 3 m depth, deposits in Klg07 characterized by relatively high calcium over titanium ratio correspond to organic-rich deposits occurring from 11.5 kyr BP to 7 kyr BP (Çağatay et al., 2000; Vidal et al., 2010). We found a similar high Ca/Ti ratio in Klg08 at 1.6 m. At shallower depths, there is a distinctive thin layer marked by a minimum in Ca/Ti ratio in cores Klg08, Klg07, Klg06 and Klg04 (red layer in Fig. 8-part a). This layer has a particular geochemical signature characterized by an anomalous Rb peak in Klg08, Klg06 and Klg04, associated with high Zr and low Ca intensities. This anomalous marker present from the Tekirdağ Basin to the Çınarcık Basin is interpreted as a key correlation marker of unknown origin. At shallower depth there is another correlative layer with a high Ca/Ti ratio (yellow upper layer in Fig. 8-part a). In the uppermost part of the core section, the Ca/Ti curves still present high variations that are used to correlate laterally the different cores.

Pb, Sr, Br and Ti intensities as well as grain size also show correlative downcore variations. These variations are illustrated in Fig. 8-part b using the core Klg04 in Çınarcık Basin and the cores Klg06 and Klg07 in the Western High. The upper part of all granulometric profiles show an upward decrease in clay-sized particles coeval to an increase in silt-sized particles. The grain size increase is coeval with a step increase in lead and titanium. These recent sedimentological changes point to an increase in the allochthonous terrigenous input in the Marmara Sea. Radiocarbon dating indicates that this increase started around 1200 cal yr BC. These changes thus occurred during the so-called Beyşehir occupation phase (BOP, Eastwood et al. 1998), which was documented in Lake Manyas along the southern shore of the Marmara Sea (Kazanci et al., 2004). The phase is characterized by forest clearance, crop cultivation and arboriculture (Van Zeist et al., 1975; Bottema and Woldring, 1994). These modifications in the vegetation cover have triggered high sedimentation rates in lakes and in the southern shelf of the Marmara Sea (Kazanci et al., 2004). Since that time the anthropogenic activity in the watershed of the Marmara Sea has continuously increased. Istanbul (Byzantium) and other major Roman Cities on the Marmara shores started developing around 600 BC and expanded when Byzantium became the Capital of the Roman Empire in 300 AD. The correlative geochemical and granulometric variations in Fig. 8-part b are interpreted as related to the anthropogenic modifications of Marmara watershed. An additional argument supporting this inference is that the observed changes are traceable in the three basins of the Marmara Sea as well as in the Western High.

The correlation of cores Klg02 and Klg05 in deep depocenters with other cores is more difficult due to the occurrence of two thick turbidites layers which distort the signal. The step increase in lead related to the BOP can still be identified in both cores as well as correlable variations in Ca/Ti ratio, Br, Ti, Sr intensities (Fig. 8-part c).

The correlable variations of Ca/Ti ratio, Pb , Br, Ti, Sr intensities and granulometry in different cores are used as chronological markers and allow looking at the synchronicity of identified events. The correlation of the different cores based on XRF matching for all the studied cores is presented in Fig. 10. This correlation is used to derive the results presented in the following sections.

5.2 Depositional pattern and sedimentation rates in the different basins and high

The correlation of the Klg cores spanning the two main sedimentary basins of the Marmara Sea and its Western High allows drawing conclusions regarding the depositional pattern.

Radiogenic lead data provide a consistent picture of the rate of hemipelagic sedimentation in the eastern and central part of the Marmara Sea. The rates are higher in the basins than on adjacent ridges. The highest value obtained in the Tekirdağ Basin is consistent with the rapid subsidence of the basin near the fault strand described in Seeber et al. (2004), and with specific locations of the cores Klg05 and Klg08 near the basin margins providing continuous terrigenous input.

The mean sedimentation rate can also be inferred since the beginning of the Beyşehir occupation phase marked by a step increase in lead at 1200 cal. yr BC, 2.85 m and 3 m of cumulated sediments have been deposited in the Tekirdağ Basin at the location of Klg05 and in the Central Basin at the location of Klg02. The average sedimentation is around 0.09 cm/yr and is dominated by turbiditic deposits representing about 80% of the sediments. The hemipelagic sedimentation rate cannot be extrapolated to obtain meaningful results by removing turbidite thickness. Most turbidites have an erosive base visible in the X-Ray images. Their emplacement in the basins is thus associated with efficient sedimentary remobilization characterized by sea floor erosion and incorporation of a significant part of the contemporary sea floor. An extreme case is Klg08 core located at the foot of the Tekirdağ slope like Klg05 but on the hanging wall of the Tekirdağ Fault. The hemipelagic rates at the Klg08 and Klg05 sites are similar, but the mean sedimentation rate in Klg08 is more than three time lower than in Klg05. Turbidites are highly erosive at the Klg08 site and are deposited preferentially further north on the down-thrown side of the fault, a local topographic low repeatedly created by earthquake rupture along the Tekirdağ Fault. A similar conclusion was reached by Beck et al. (2007) in the Central Basin.

In the Western High, the mean sedimentation rates of cores Klg06 and Klg07 are three times lower than in the Tekirdağ Basin during the period characterized by high lead intensities starting respectively at the depth of 1.2 m and 0.8 m (Fig. 8-part b). This is in agreement with the lower hemipelagic rate and the thin fine-grained turbidites deposits.

Finally, the two consecutive thick turbidites recorded both in the Tekirdağ and the Central Basin are anomalously large compare to the other turbidites identified and are reminiscent of the homogenites deposited in the lower (pre-Holocene) lacustrine sequence during a period of high terrigenous accumulation rates on the edges of the Marmara Sea (Beck et al., 2007). The occurrence of these thick turbidites suggests a temporary increase in terrigenous sediment supply that would occur after the Beyşehir occupation phase. Once a significant part of the forest cover has been removed and that large scale urbanisation started, erosion and increased sedimentary transport occurred in the Marmara watersheds. Sediment supply to the Marmara shelves thus increased and larger turbidites were deposited. As the watershed adjusted to the changed environment, sediment supply gradually decreased, and thinner turbidites were deposited. These inferences suggest that the thickness of turbidites in the Marmara Sea is controlled by the amount of cumulated unstable sediments on slopes between earthquakes as well as by the strength of earthquake shaking.

5.3 Turbidites triggered by the 1912 historical earthquake

The $^{210}Pb_{xs}$ data provide a chronology of the most recent sedimentary events and thus, allow characterizing turbidites triggered by the 1912 M=7.4 Mürefte earthquake.

The rupture associated with the 1912 earthquake was documented onland west of the Marmara Sea (Rockwell et al., 2009; Aksoy et al., 2010) and offshore on the Tekirdağ Fault (Armijo et al., 2005; Aksoy et al., 2010). Figure 7 indicates that the most recent mass wasting event called e1 recorded in cores Klg02, Klg05, Klg08, Klg06, Klg07 occurs at a depth where $^{210}Pb_{xs}$ levels reach minimal meaningful values (10 to 20 mBq.g^{-1}). Considering the interface $^{210}Pb_{xs}$ activities of nearby ROV (140 to 170 mBq.g^{-1}), and its half-life of 22.3 years, the low values of $^{210}Pb_{xs}$ just above the level of the most recent mass-wasting event would occur 4-5 half-lives or 80 to 100 years. The most recent turbidites in the Tekirdağ Basin and in the Western High are thus interpreted to be related to the 1912 earthquake.

The 1912 turbidite in Klg05 and Klg08 cores has two basal sandy layers, which is a characteristic of turbidites deposited at the Klg05 site in the Tekirdağ Basin. The earthquake has also left a sedimentary imprint in the Central Basin, which suggests that the rupture of the Tekirdağ Segment can generate turbidites in the Central Basin. This implies that the two different depocenters of the Marmara Sea, which are the Tekirdağ and the Central Basins, may have the potential to record the same large magnitude earthquake.

5.4 Origin of turbidites

The most recent turbidite in the studied cores have been generated by the 1912 earthquake, and one can wonder if other identified turbidites have a seismic origin. Sediment gravity flows can be produced by a wealth of other processes like storm, wave loading, tsunamis, and sediment loading (Adams, 1990; Goldfinger et al., 2003b). Seismoturbidites have often particular sedimentological imprints like multiple coarse bases indicating multiple sources (Nakajima and Kanai, 2000; Goldfinger et al., 2008), complex laminations (Shiki et al., 2000; McHugh et al., 2011), flaser beds which are tractive current-induced structures that can be related to seiche motion (Beck et al., 2007), erosional contacts, grain-size breaks and abrupt changes in sedimentary structure (Nakajima and Kanai, 2000; Shiki et al., 2000). They can also have a particular geochemical imprint (Nakajima and Kanai, 2000) with an increase in terrigenous sediment content (McHugh et al., 2011). These criteria are met for all turbidites in Klg05 and most in Klg02 (see section 4.2). The two coarser basal pulses observed in majority of turbidites in Klg05 are probably related to flow through separate channels that amalgamate at the site located near the base of the basin slope. However, as stated by Masson et al. (2011) it is difficult based on sedimentological criteria alone to recognise without ambiguity seismically-generated turbidites. Another key test, commonly used in paleoseismology, is to check the synchronicity of the documented events at different sites within a given structural setting (Goldfinger, 2011). In the following, the synchronicity test is applied to the Kullenberg and the published cores. The test relies on the core correlation obtained by using lithological descriptions, χ, XRF, granulometric data, radiocarbon and ^{210}Pb dating.

In the Tekirdağ Basin, Klg05 was compared to 1) the C8 core (McHugh et al., 2006) located 3 km north, 2) the Klg08 core located 6 km west, 3) the MAR97-02 (Hiscott et al., 2002) located 6.6 km north, and 4) the MD2432 located 6.7 km west (Fig. 1). The 110 cm long C8 core is too short to sample the deep thick turbidites, nevertheless there is still a tie between the cores (Fig. 15 in the appendices). The comparison between Klg05 and Klg08 is not straightforward because of the highly compressed sedimentary record of Klg08 (Fig. 11 and 15 in appendices), but there is still a clear correspondence between event 4 (56 cm) in Klg08 and event 4 (100 cm) in Klg05 and between event 2 (41 cm) in Klg08 and event 2 (48 cm) in Klg05 (Fig. 15). At greater depth, the two main amalgamated turbidites around 70 cm depth in the core Klg08 correspond to the two largest turbidites (events 5 and 6) in Klg05. They show multiple pulses and erosional cut-outs that suggest seismic triggering (Nakajima and Kanai, 2000; Shiki et al., 2000). Due to the lack of high resolution data the comparison with MAR97-02 core (Hiscott and Aksu, 2002) is difficult. Nonetheless this core, located 6.5 km to the north (Fig. 1), presents two coarser intervals at 70-110 cm and 140-185 cm depths that could correspond to the two large events e5 and e6 documented in Klg05 (Fig.15 in the appendices). In addition, radiocarbon ages dating are identical for the e5 turbidite and for the coarser layer at 70-110 cm in the MAR97-02. Finally, the MD2432 core can be correlated to the Klg05 core based on the χ measurement. Density data also indicate turbiditic events that would correspond to events 3 to 6 in Klg05.

In the Western High, fine-grained turbidites recorded in cores Klg06 and Klg07, 15 km apart, can be easily related because they have similar geochemical profiles (Fig. 8). In both cores, almost a one-to-one correspondence between turbidites is recorded. The two largest turbidites e5 and e8-e7 in Klg06 and Klg07 are correlative and are marked by a distinctive strong terrigenous signature in sand, Zr, χ (Figs. 6 and 15). Silty turbidites in the Western High are dissimilar to the slump-induced turbidites present in the Tekirdağ and Central Basins, but they can have a common seismic origin. Indeed, M >7 earthquakes on the Tekirdağ Segment can trigger sandy turbidity currents in the basin and a muddy suspension cloud, which would deposit a very fine-grained distal turbidite layer in the High (Inouchi et al., 1996; Shiki et al., 2000). So our final test is to look if sandy turbidites in the Tekirdağ Basin are synchronous with silty turbidites in the Western High (Fig. 10). The XRF correlation implies that the two largest turbidites e5 and e6 in Klg05 correspond to the distinctive distal turbidites e5 and e8-e7 in Klg06 and in Klg07 on the Western High marked by sand, Zr, χ peaks. Furthermore, a similar number of turbidites are identified in cores above the time horizon underlined in red in Fig.10. Both observations suggest synchronicity of the turbidites in Tekirdağ and in the Western High. The suspension cloud responsible for the fine-grained turbidites must be at least 400 m thick as the Klg06 site is about 400 m higher than the Klg05 site. Shiki et al. (2000) state that the plumes associated to earthquake triggered turbidites are higher and thicker that the usual suspension clouds derived from canyon flow turbidity currents. Furthermore McHugh et al. (2011) detected an unusual 600 m thick sediments plume still present almost 2 months after the M=7.0 Haïti earthquake. The occurrence of distal turbidites and their correlation with basinal proximal turbidites suggests that both types of turbidites have been uniquely generated by earthquake shaking in the Tekirdağ Basin and not by some other natural phenomenon.

In the Central Basin, the Klg02 core is compared to core C4 (McHugh et al., 2006) and to core MD2429 (Beck et al., 2007). The two largest turbidites e3 and e4 recorded in Klg02 were documented at the same depth in the core C4 of McHugh et al. (2006) (Fig. 1). Additionally, two deeper organic rich layers in C4 can be correlated with the e6 and e7 events of Klg02 (Fig. 15). In the nearby core

MD2429 the magnetic susceptibility record of the first 6 metres (Beck et al., 2007) is identical to the magnetic susceptibility data of the Klg02 core with two peaks framing low values (Fig. 15). These two peaks correspond to the two main sandy layers forming the base of events e3 and e4. The relative low values match with the main body of the second homogenite (Fig. 5). The density data of MD2429 core allows identifying other major turbidites in the cores which corresponds to events 5, 6 and 7 in Klg05. Turbidites in the Central Basin have thus significant lateral extension. We infer that they also have a seismic trigger.

6 Paleoseismological implications

The sedimentary cores studied provide a paleoseismological record of the Tekirdağ Fault ruptures. The 1912 Mürefte earthquake (event 1) is recorded in the Tekirdağ Basin and in the Western High as well as in Central Basin where it has a faint expression. Considering the 14C age of 2185 yr BP below event 6 in Klg05 with the reservoir correction of 340-460 years proposed by McHugh et al. (2006), the mean recurrence time of events along the Tekirdağ Fault would be about 300 years. Combining all radiocarbon ages dating obtained in cores from the Tekirdağ Basin and an average reservoir correction of 450 years, we can propose the following possible match between sedimentary events and historical earthquakes (Ambraseys, 2002): events 2 to 5 could correspond, respectively, to events occurring in 1766, 1354 or 1343, 1063, 557 and 437. The obtained paleoseismological record might not be complete. The triggering of seismoturbidites also depends on the availability and volume of unstable sediments that accumulate on the basin slopes.

The inner Central Basin (Klg02) located between the Tekirdağ and the Central Faults (Fig. 1) can also record mass-wasting events synchronous with the Tekirdağ Basin. The first example is the 1912 disturbances triggered by the rupture of the Tekirdağ Fault. An other example is the top turbidite in the Central Basin (event 3-Klg02) which seems synchronous with the shallowest turbidite in the Tekirdağ Basin (event 5-Klg05; Figs. 8 and 10). The latter implies massive slope failures both in Tekirdağ and Central Basins. It might have been triggered by the Tekirdağ fault rupture alone, but was most probably triggered by the quasi-synchronous rupture of the Tekirdağ and Central Faults. Such rupture scenario may have happened during the M= 7.1 May 1766 and M=7.4 August 1766 earthquake sequence as modelled in Pondard et al. (2007).

Another noticeable paleoseismological result is the relatively low number of turbiditic events recorded in the Central Basin, which could record earthquakes rupturing the Tekirdağ and Central Segments. It might be a site effect as the Klg02 core is situated 14 km away from the basins slopes and only large mass wasting events can be recorded. In addition, even if sediment supply on the shelf and slope of the Central Basin is similar to the Tekirdağ Basin, there might not be enough sediments available to trigger turbiditic mass flow in the inner basin each time there is a M>7 earthquake on the Central or Tekirdağ Faults. An other possible explanation would be frequent ruptures of the Central and Tekirdağ Segments in sequence or as a single through-going rupture. In these cases, we would have indistinguishable coeval turbiditic deposits in both basins. The last possibility would be a less frequent earthquake rupture of the Central Segment that would be related to partial creep along that specific segment. Partial creep would mean lower recurrence rate and maximum magnitude on the Central Segment than on the other NAF Segments. More sedimentary records from the Central Basin are needed to resolve that key question, which have fundamental consequences on earthquake recurrence rate and earthquake magnitude.

Conclusions

The combination of X-ray imagery, XRF scanning and high-resolution granulometric measurements performed on five cores has documented the cyclic occurrence of instantaneous sedimentary events deposited in the Marmara Sea as well as global sedimentation changes that can be used to relate the different records. Radiocarbon age dating suggests that about eight major turbiditic events occurred in the Tekirdağ Basin and seven in the Central Basin in the last 2500 years.

Turbiditic events appear to be reliable paleoseismological indicators of ruptures of the Tekirdağ Fault. This interpretation is first based on (1) specific XRF and grain size characteristics, (2) synchronicity of turbiditic events identified in different cores and (3) correlative proximal sandy turbidites in the basins with distal fine-grained turbidites in the high. The most straightforward triggering mechanism for coeval distal and proximal events is shaking induced by earthquakes breaking the Tekirdağ Segment of the North Anatolian Fault. The relatively low number of turbidites documented in the Central Basin compared to the Tekirdağ Basin might be linked to ruptures in close sequence on the Tekirdağ and Central Segments like in 1766 (Pondard et al., 2007) or to creeping along the Central Segment. A link is also proposed between the first observed sedimentary event and the M=7.4 1912 Mürefte earthquake. This earthquake that last activated the Tekirdağ Fault left a distinct imprint in all cores. Finally, more effort must be achieved to obtain reliable age model of the sedimentary cores, which would allow a better understanding of the seismic cycle of the different NAF Segments crossing the Marmara Sea.

Acknowledgements

We first would like to thank reviewers R. Hiscott, N. Çağatay and the two other anonymous reviewers for their in depth comments, which improve very significantly the paper. We also thank Rolando Armijo who was the scientific director of the Marmarascarps Marine campaign in 2002 from which the studied cores were collected. We acknowledge Jean-Luc Schneider for his valuable help in core logging. We are grateful to Isabelle Billy, Joël Saint-Paul and Olivier Ther for core sampling, realisation of X-ray scanner imagery, XRF data preparation and acquisition as well as Elisabeth Michel and Elisabeth Tellier for their help on foraminifers extraction. Radiocarbon dating was supported by the CNRS-INSU Artemis program and done in the Artemis LMC14 laboratory. The program CNRS/FRS-FNRS CGRI supported granulometric data acquisition in Liège (Belgium) and the ENS, UMR8538 provides additional financial support for data acquisition. Finally, we would like to thank Christian Beck for the fruitful discussions.

Figures

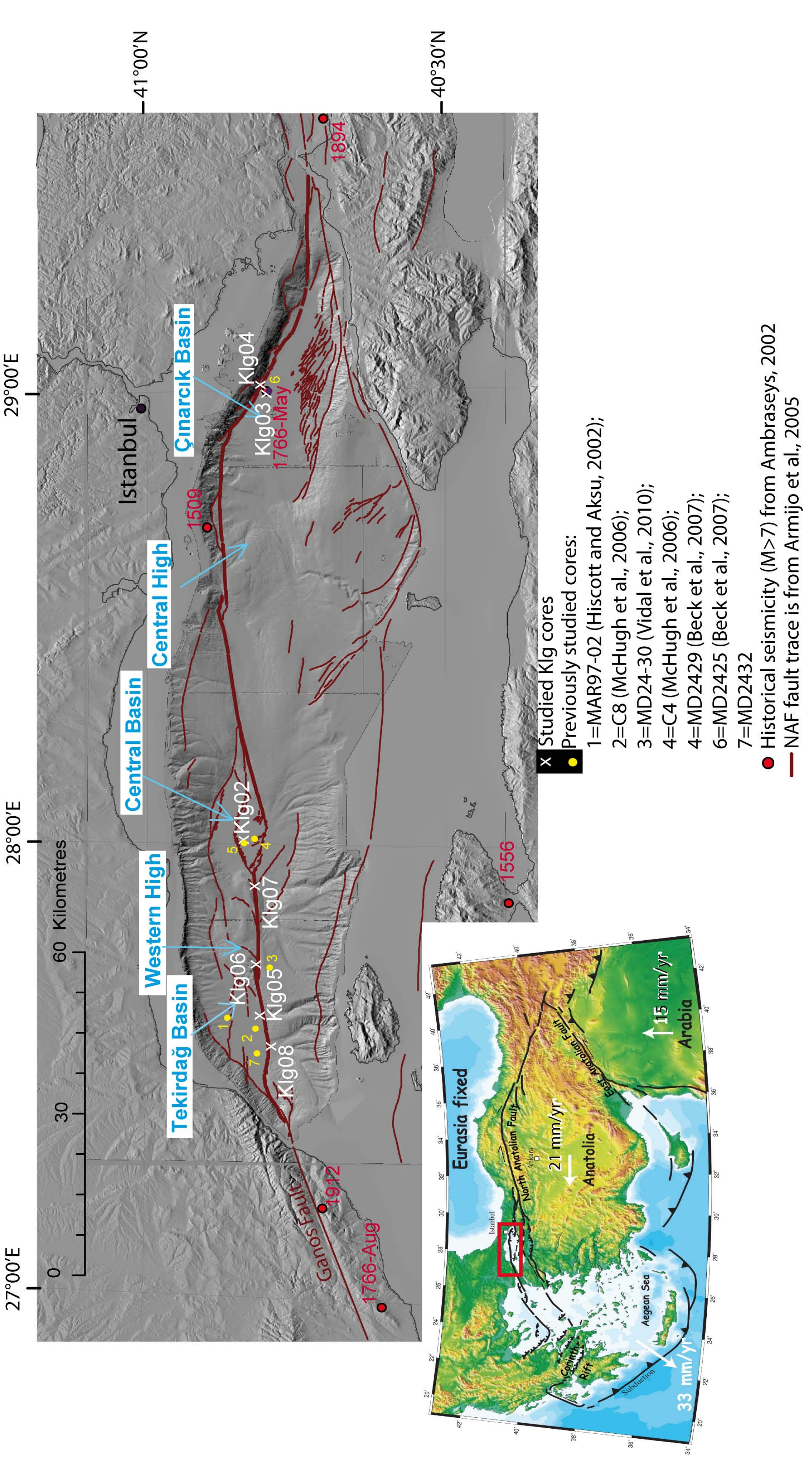

Figure 1: General context of the Marmara Sea crosses by the North Anatolian Fault (NAF). Main structures are labelled in blue. Global tectonic context of the Anatolian Plate is included as inset with GPS velocities from Reilinger et al. (2006), with a red box indicating the location of Fig.1.

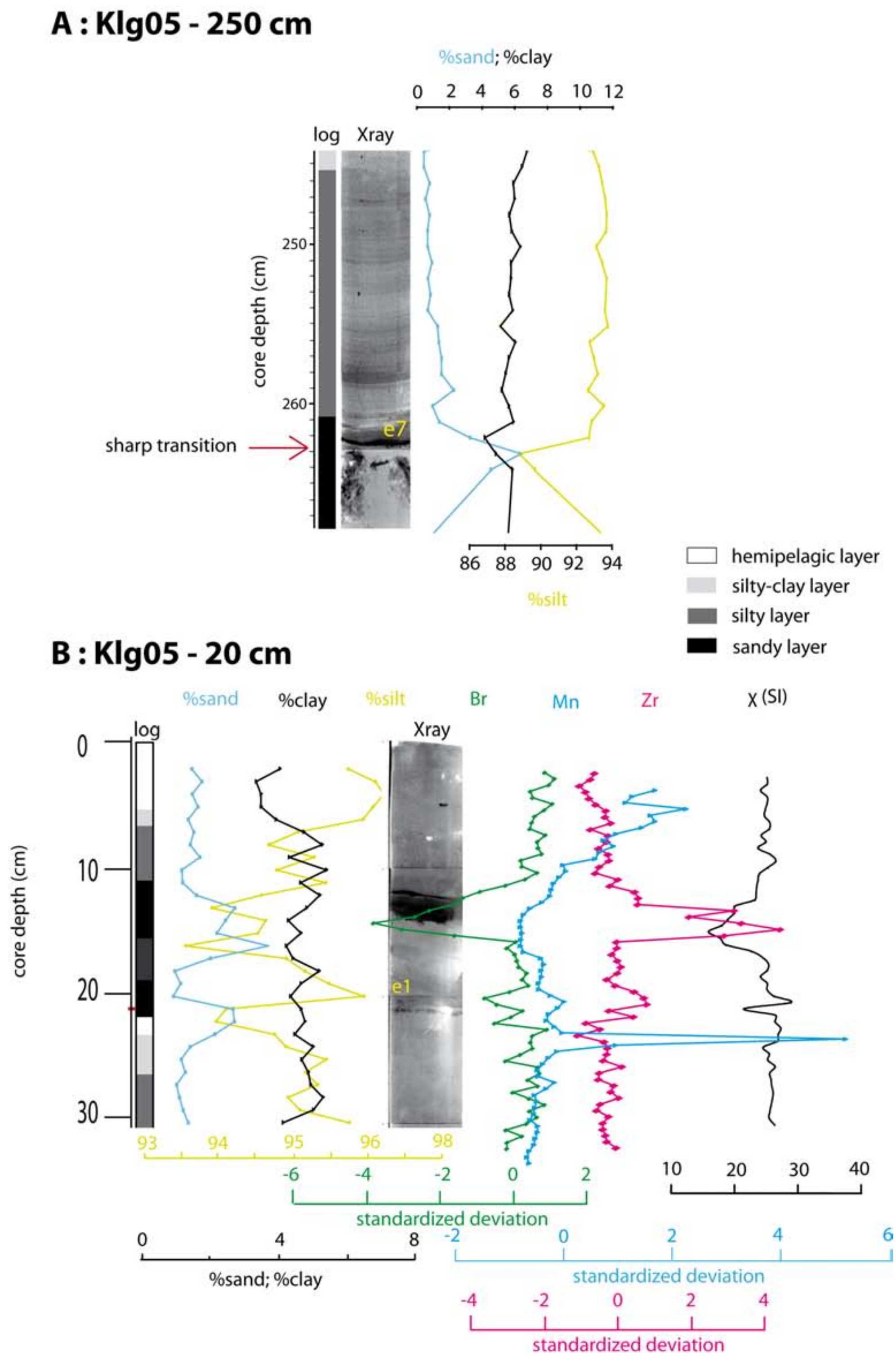

Figure 2: Typical examples of turbidites: granulometric and geochemical signatures as described in Sec.4. Turbidites are composed of a basal sandy layer, an upper silty unit with frequent laminations and a top light grey clayey unit. A : X-ray imagery and granulometry zooms of event 7 in Klg05. Yellow label on the X-ray indicates the position of the event as in Fig. 4. B : X-ray imagery, granulometry and geochemical profiles of event 1 in Klg05. Turbidites can have a positive signature in Zirconium (pink curve), negative in bromine (green curve) and just below turbidites Manganese (blue curve) typically shows a peak. Yellow names indicate events as referenced in Fig.4.

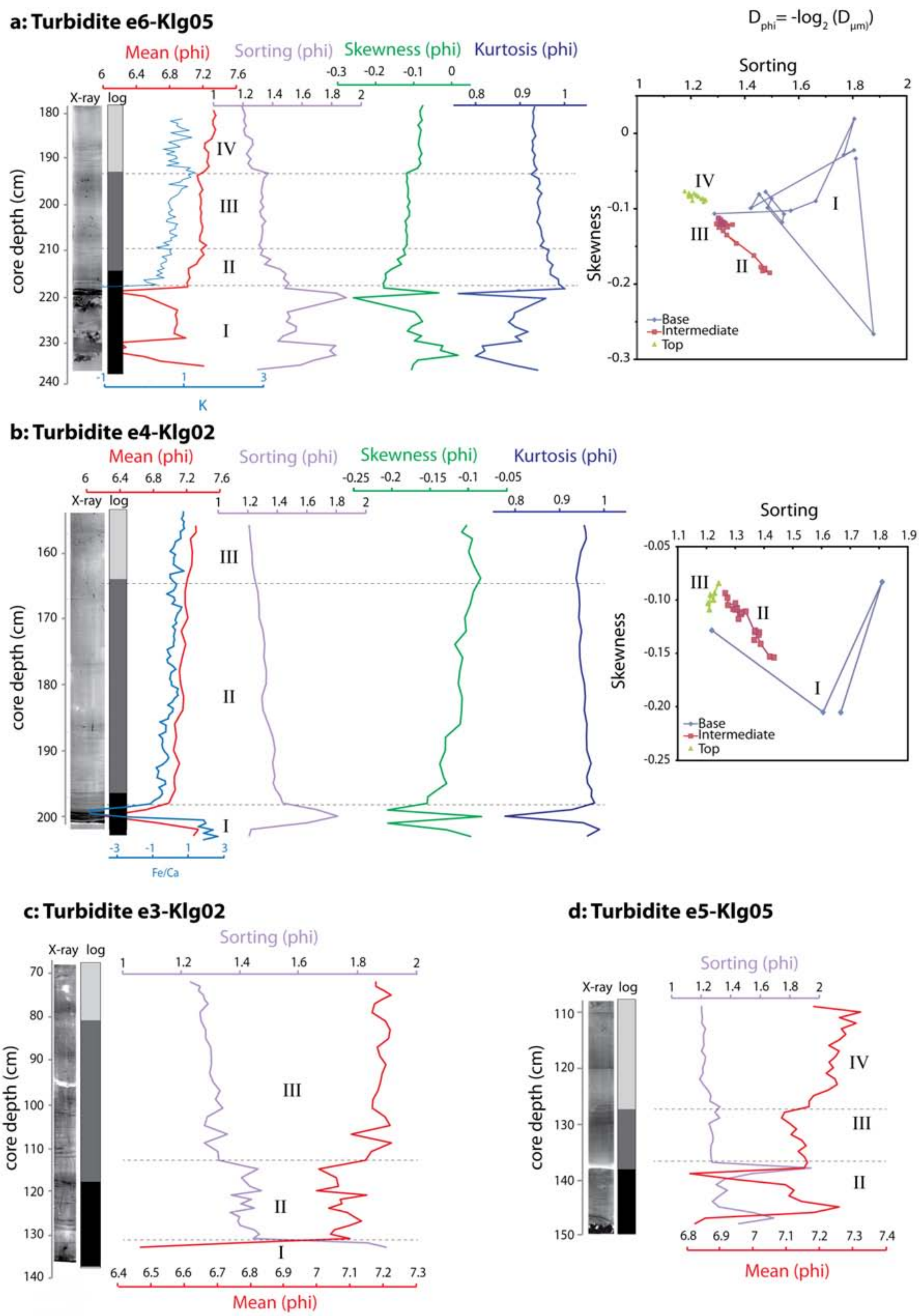

Figure 3: Characteristics of the thickest turbidites in Klg02 and Klg05 cores by using X-ray, log, grain size and geochemical parameters.

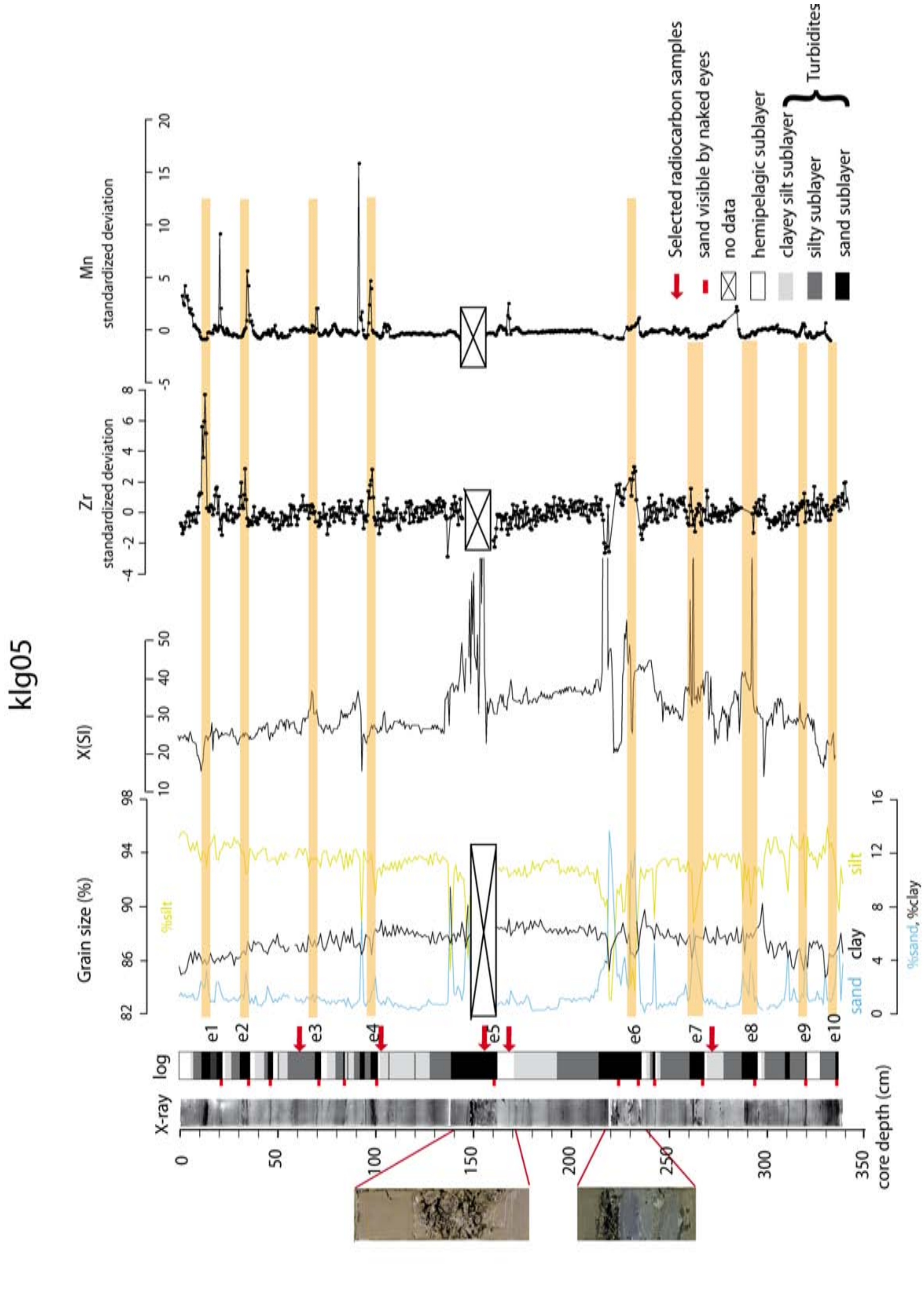

Figure 4: Stratigraphic log of the Klg05 core in the Tekirdağ Basin obtained combining X-ray imagery, grain size, magnetic susceptibility data, Mn and Zr standardized intensities. On the left, zoom pictures of the two basal layers of the thickest turbidites with gravel are presented. Main turbidites deposited are identified and labelled; event label is changing according to their stratigraphic position, beginning with 1 at the top of the core. In black is represented the sandy dark layer, in grey the intermediate silty layer, in light grey the upper clay-rich layer and in white the background sedimentation.

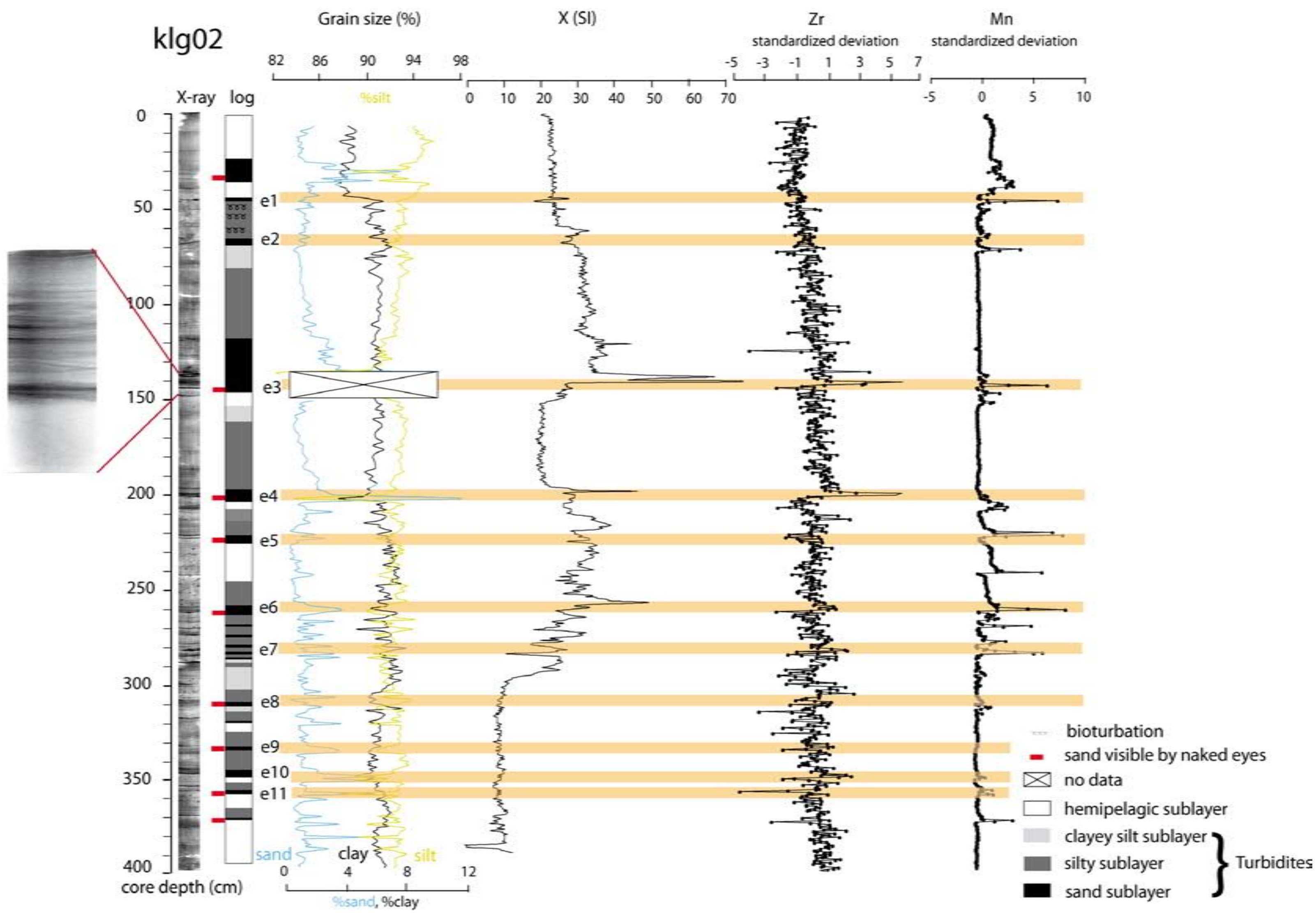

Figure 5: Stratigraphic log of the Klg02 core in the Central Basin obtained combining X-ray imagery, grain size, magnetic susceptibility data, Mn and Zr standardized intensities. On the left, zoom in the X-ray of the basal layers of the thickest turbidite e3 with complex laminations. Main turbidites deposited are identified and labelled; event label is changing according to their stratigraphic position, beginning with 1 at the top of the core. In black is represented the sandy dark layer, in grey the intermediate silty layer, in light grey the upper clay-rich layer and in white the background sedimentation.

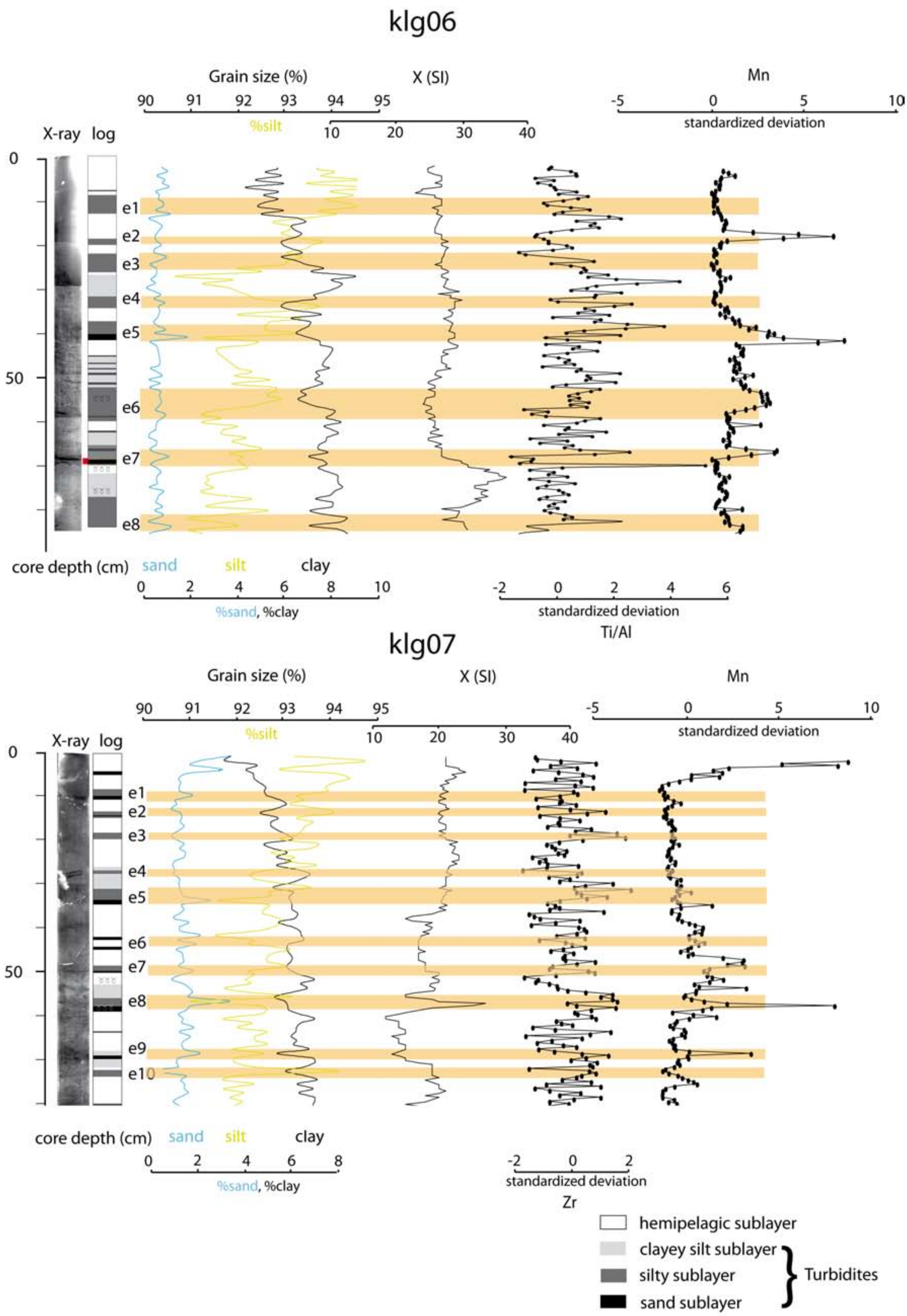

Figure 6: Stratigraphic log for the first 80 cm of the klg06 and Klg07 cores situated in the Western High Ridge obtained combining X-ray imagery, grain size, magnetic susceptibility data, Mn and Ti/Al or Zr standardized intensities. Main events deposited are identified and labelled; event label is changing according to their stratigraphic position, beginning with 1 at the top of the core. The complete stratigraphic logs are presented in the appendices (Figs. 12 and 13)

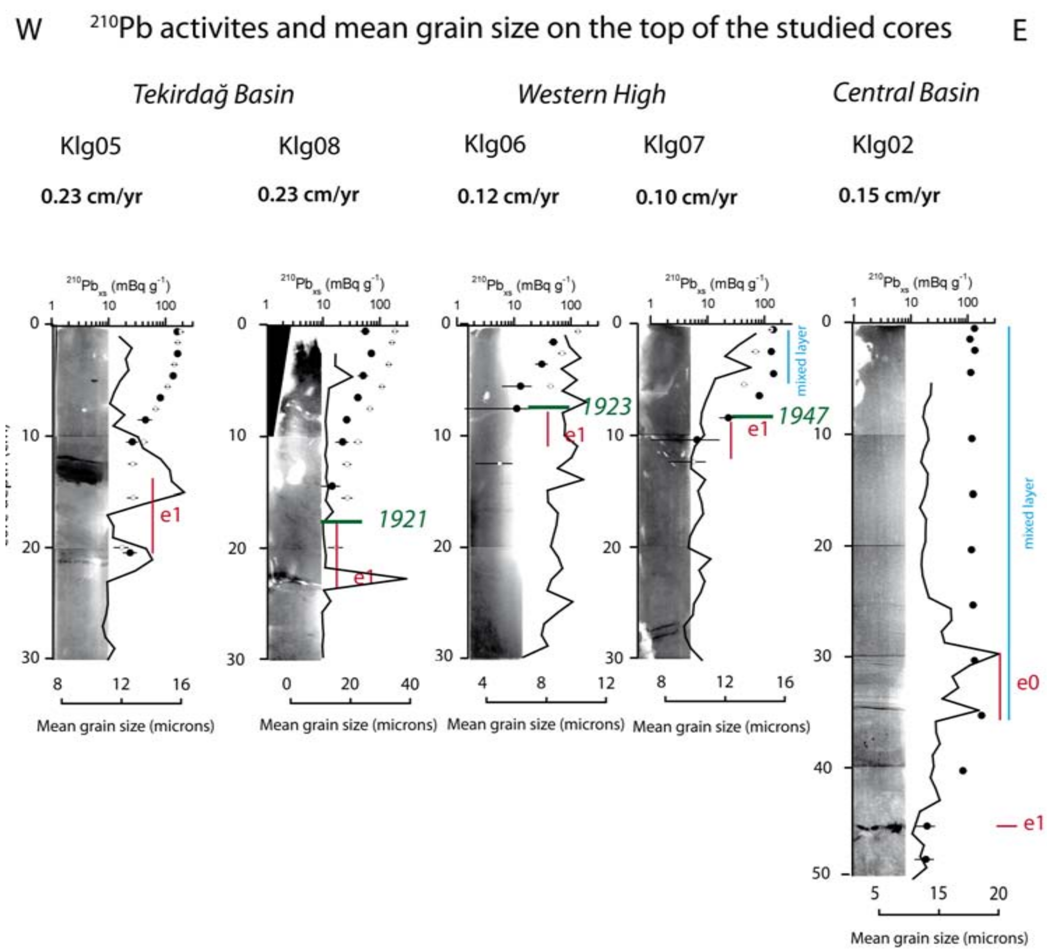

Figure 7: Excess ^{210}Pb activities (black dots) and computed sedimentation rates of the cores Klg02, Klg05, Klg06, Klg07 and Klg08. White dots are from the nearby ROV cores and show that no significant lost of sediments occurred in Klg cores. The extend of the mixed layer is indicated in blue. X-ray imagery associated to the mean grain size (black lines) show the location of the e1 sedimentary event induced by the M=7.4 1912 earthquake. The age model derived from $^{210}Pb_{xs}$ at the top of the 1912 turbidites is indicated in green. The event e1 have the following characteristics.

In Klg05, e1 is marked by two basal sandy layers at 13 and 21 cm depth suggesting two distinct mass flows. The thickest upper one is visible by eyes and associated with a significant increase in zirconium and titanium content (Fig. 4). In Klg08 core similar sandy layers and geochemical signatures are observed at 18 cm and 23 cm depth. In Klg07, the event is marked at 10-11 cm by a small sandy peak, a step increase in silt and an increase in Ti-Mn XRF. In Klg06, there is a similar step increase in silt associated to a dipping white line in the X-ray.

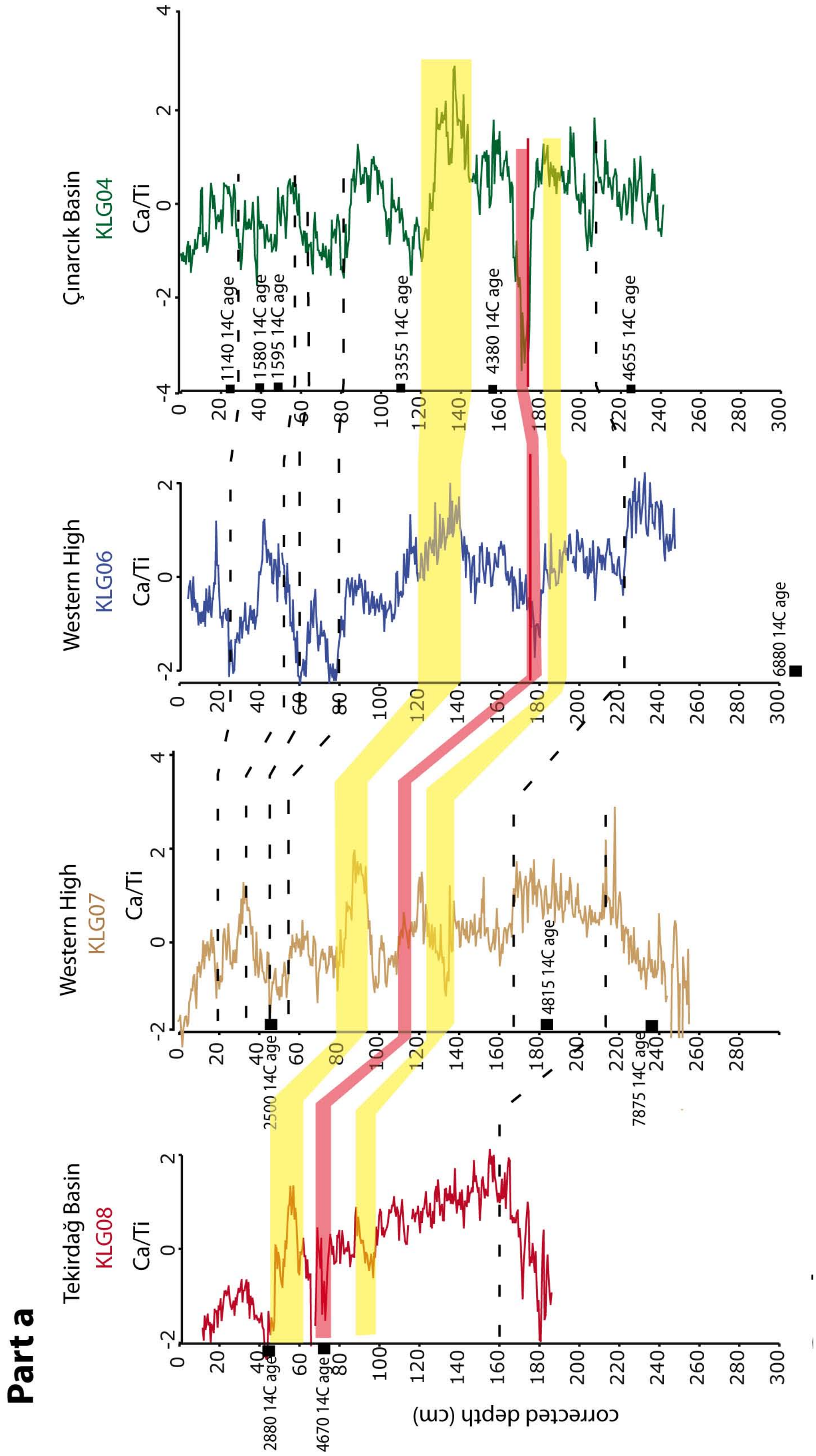

Part a
Tekirdağ Basin
KLG08
Western High
KLG07
Western High
KLG06
Çınarcık Basin
KLG04
Ca/Ti
corrected depth (cm)
2880 14C age
4670 14C age
2500 14C age
4815 14C age
7875 14C age
6880 14C age
1140 14C age
1580 14C age
1595 14C age
3355 14C age
4380 14C age
4655 14C age

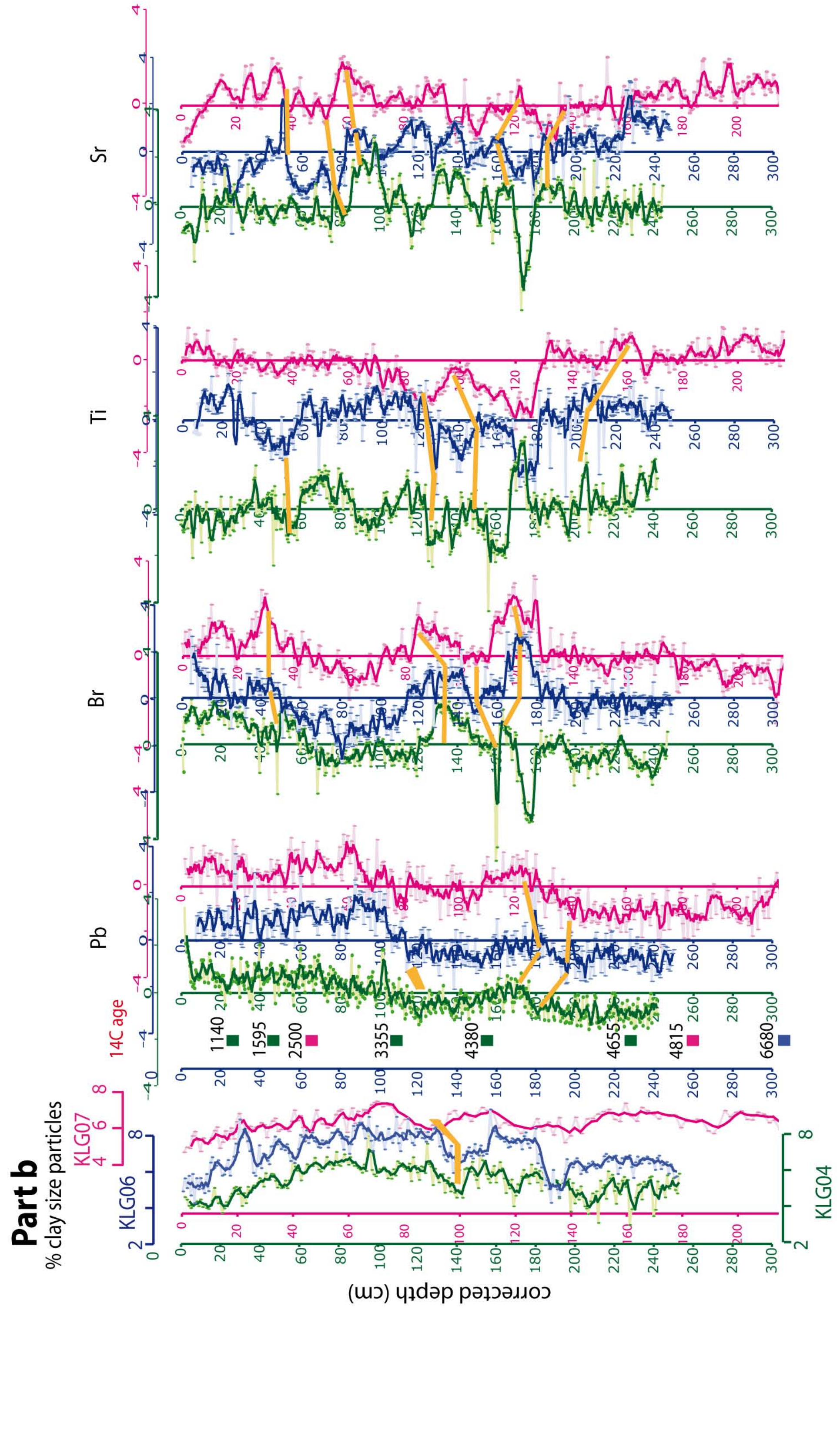
Part b
% clay size particles
KLG07
KLG06
KLG04
corrected depth (cm)
14C age
1140
1595
2500
3355
4380
4655
4815
6680
Pb
Br
Ti
Sr

Part c

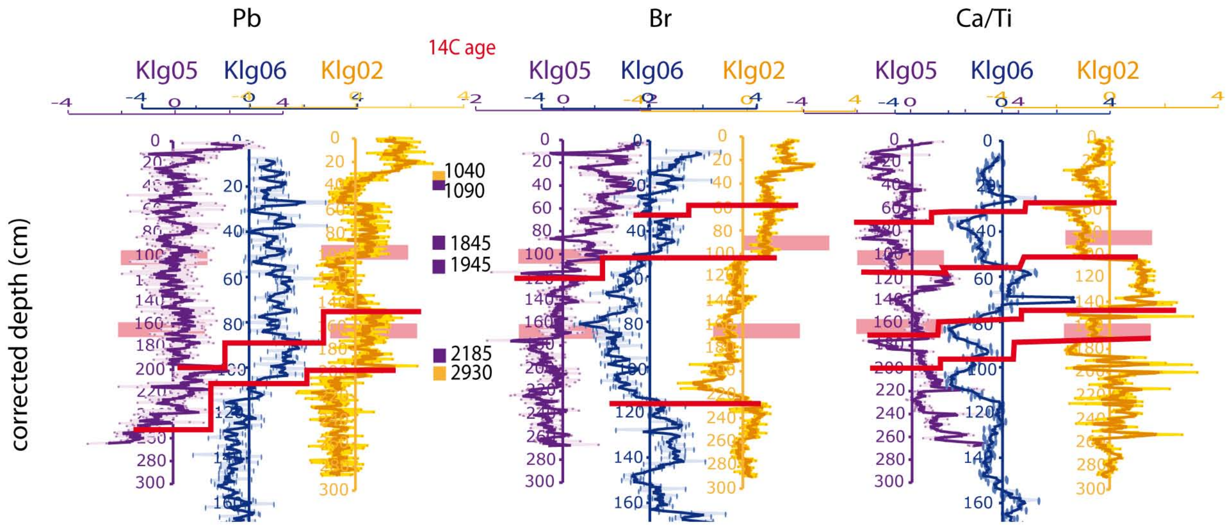

Figure 8: Correlation of different cores based on XRF and granulometric data. All basal sandy layers have been removed. **a**: Ca/Ti ratio profiles for cores Klg08 (red curve), Klg07 (brown curve), Klg06 (blue curve) and Klg04 (green curve). Uncalibrated 14C yr BP are indicated on the left of the profiles (Table 2). Dashed black lines represent correlative highs or lows. **b** Profiles from left to right of clay-sized particles and of the standardized XRF data for Pb, Br, Ti and Sr for cores Klg04 (green curve), Klg06 (blue curve) and Klg07 (pink curve). Bold orange lines represent correlative highs or lows. **c** Profiles of the standardized XRF data with from the left to the right Pb, Br and Ca/Ti ratio for the cores Klg02 (yellow curves), Klg05 (purple curves) and Klg06 (blue curves). Bold red lines represent key points of correlation. Pink rectangles indicate the location of the top fine grained of the largest turbidites in Klg05 and Klg02.

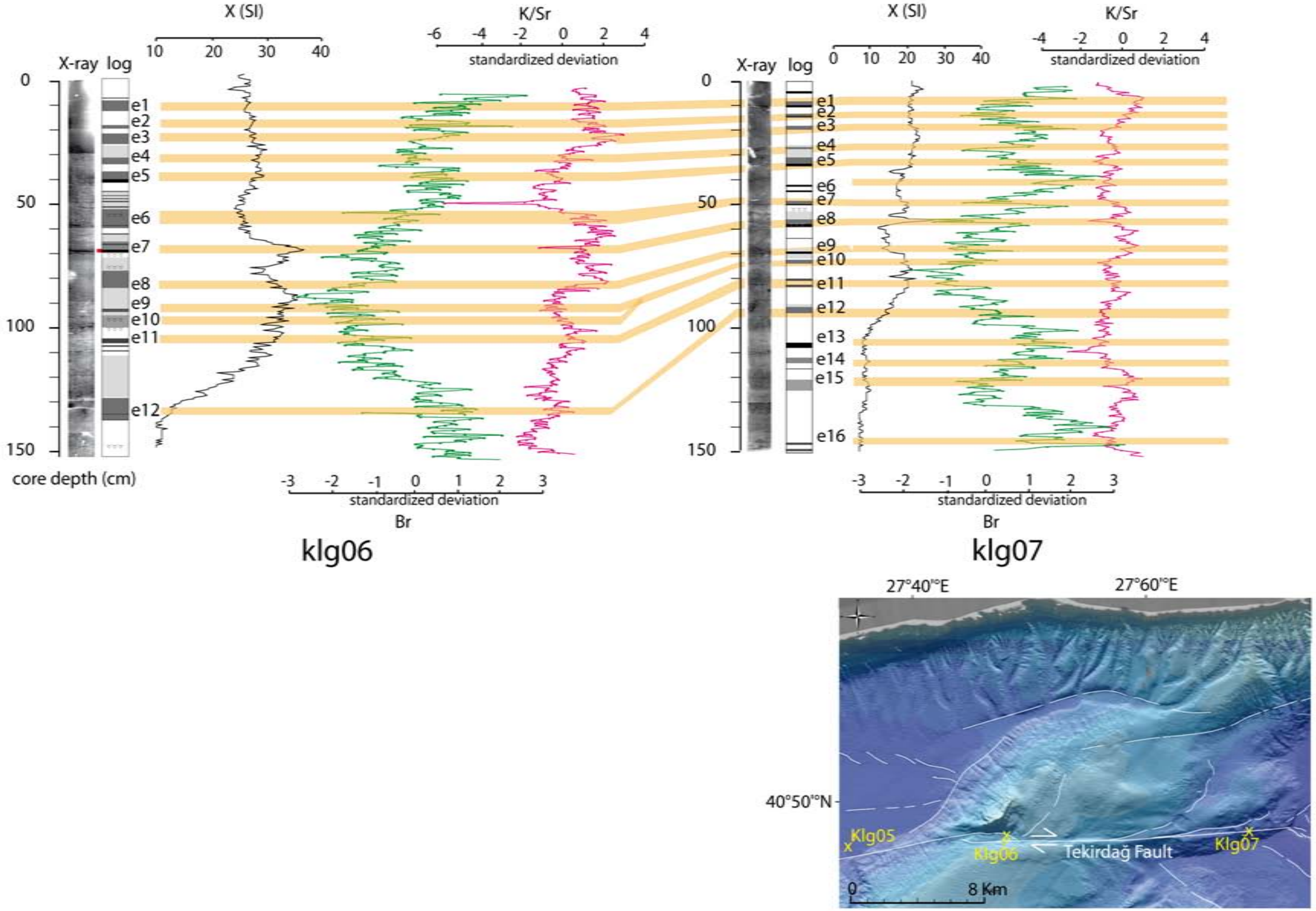

Figure 9: Core correlation between Klg06 and Klg07 using X-ray, magnetic susceptibility, bromine and K/Sr ratio. Increase Sr at the base of turbidites suggests allochthonous input. In opposition, increase in K might reflect higher illite content in the upper clayey silt sublayer. Localisation of the cores is indicated on the inset map.

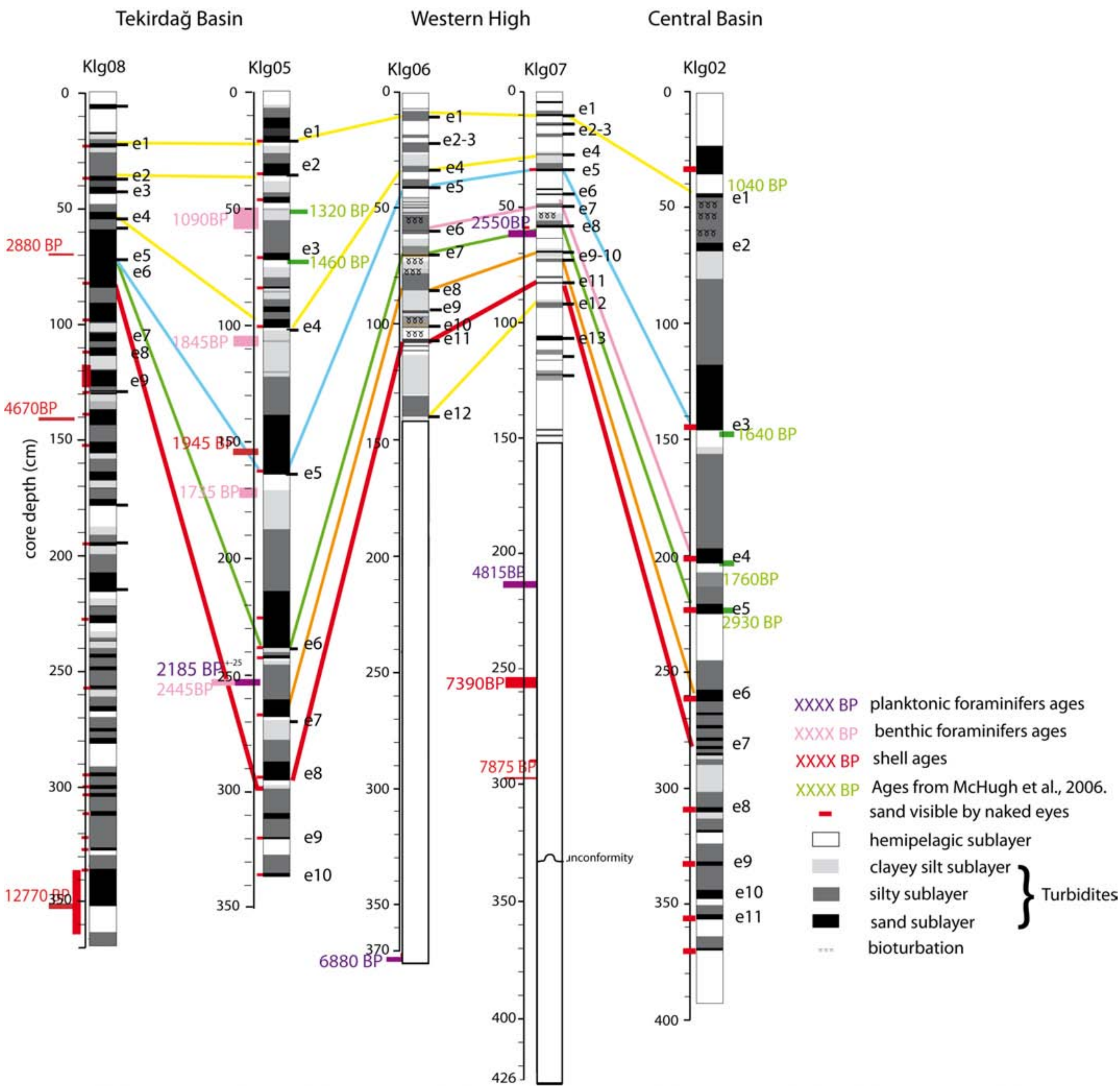

Figure 10: Correlation obtained from XRF data (Fig. 8) for the cores Klg08, Klg05, Klg06, Klg07 and Klg02. Lines between cores represent the correlative sedimentary events identified in Figs. 4, 5, 9. Uncalibrated radiocarbon ages (not calibrated) for shells (in red), planktonic foraminifers (in purple), benthic foraminifers (in light rose) are presented in Table 2. The radiocarbon ages in green are from McHugh et al. (2006).

Table 1: Location of Kullenberg cores collected during the Marmascarps mission in 2002

Basin	Core	Latitude (°N)	Longitude (°E)	Water depth (m)	Core length (cm)
Tekirdağ	klg05	40°48,50	27°37,3	1123	341
Tekirdağ	klg08	40°47,31	27°33,22	1111	385
Western High Ridge	klg06	40°48,90	27°44,28	726	371
Western High Ridge	klg07	40°49,115	27°54,44	1065	432
Central	klg02	40°50,28	28°00,54	1266	403

Table 2: AMS Radiocarbon dating results performed on bivalve shell fragments (sh), bulk sediment (TOC+TIC) (bk), benthic (bf) and planktonic (plc) foraminifers. Sample name written in italic are samples considered to be reworked and were not used for the interpretations. Analyses were performed at Artemis LMC14 laboratory and AEON laboratories; 14C dating have not been calibrated and corrected for reservoir effect.

Sample	**Type**	**Age (yr BP)**	**error (± yr)**
Klg02, 180 cm	bk	4830	20
Klg02, 185 cm	bk	3430	20
Klg02, 352 cm	bk	5060	20
Klg03, 114 cm	plc	2380	15
Klg03, 114 cm	bf	1630	30
Klg03, 158 cm	sh	2370	30
Klg03, 161 cm	plc	2370	60
Klg05, 48 cm	bf	1090	15
Klg05, 94 cm	bk	3070	20
Klg05, 102 cm	bk	3110	20
Klg05, 103 cm	bf	1845	15
Klg05, 146 cm	bk	3870	20
Klg05, 152 cm	sh	1945	30
Klg05, 167 cm	bf	1735	30
Klg05, 178 cm	sh	35790	330
Klg05, 217 cm	bk	5180	20
Klg05, 220 cm	sh	13700	45
Klg05, 229 cm	sh	39480	490
Klg05, 234 cm	sh	14390	50
Klg05, 250 cm	plc	2185	20
Klg05, 250 cm	bf	2445	25
Klg05, 261 cm	bk	4180	20
Klg06, 278 cm	sh	33870	270
Klg06, 366 cm	plc	6880	120
Klg07, 61 cm	plc	2500	30
Klg07, 212 cm	plc	4815	45
Klg07, 255 cm	sh	7390	30
Klg07, 297 cm	sh	7875	35
Klg08, 73 cm	sh	2880	30
Klg08, 90 cm	sh	30200	180
Klg08, 117 cm	sh	28880	150
Klg08, 124 cm	sh	12850	40
Klg08, 145 cm	sh	4670	30
Klg08, 150 cm	sh	21380	80
Klg08, 220 cm	sh	30160	180
Klg08, 326 cm	sh	39820	510
Klg08, 355 cm	sh	12770	45

appendix

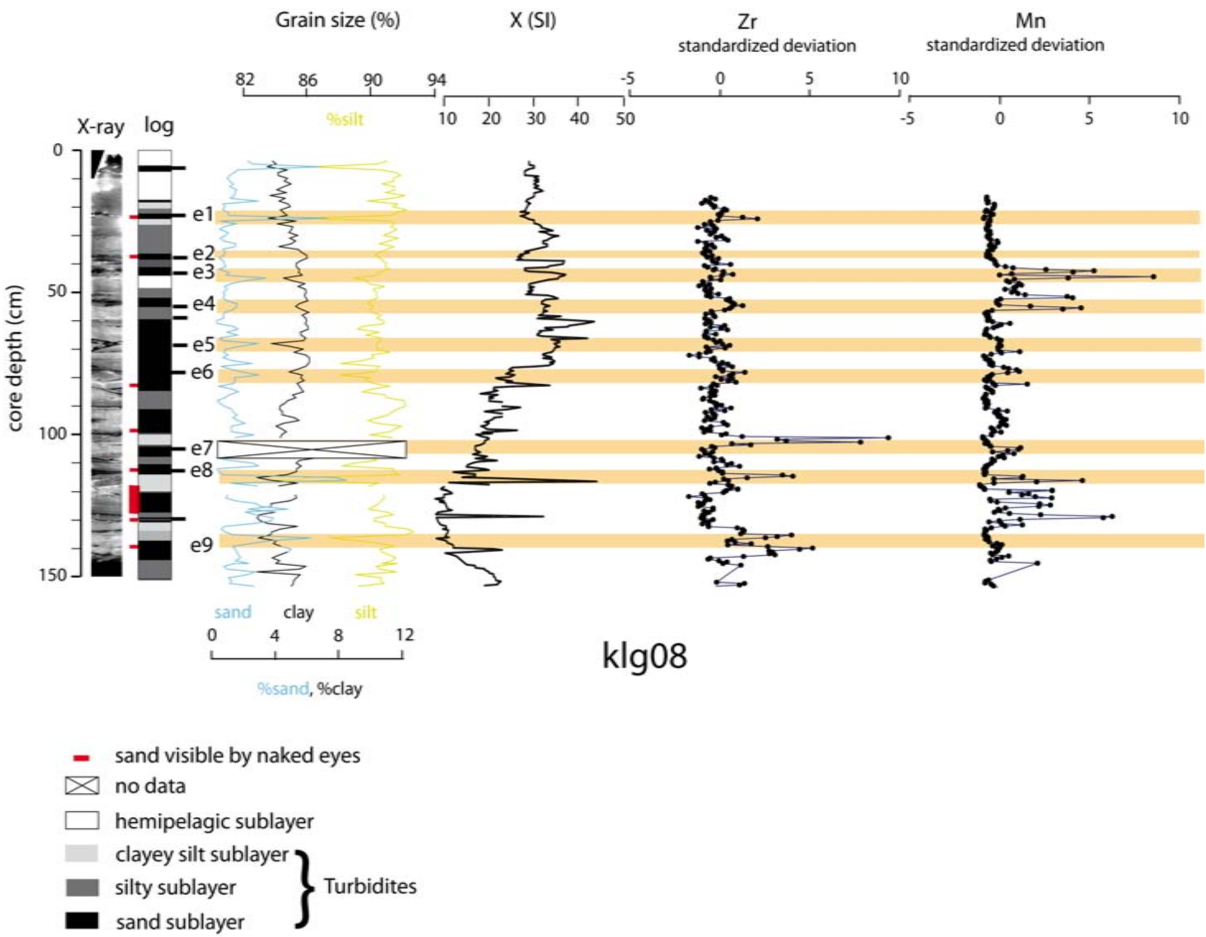

Figure 11: Stratigraphic log for the first 1.5 m of the klg08 core situated in the Tekirdağ Basin obtained combining X-ray imagery, grain size, magnetic susceptibility data, Mn and Zr standardized intensities. Main events deposited are identified and labelled.

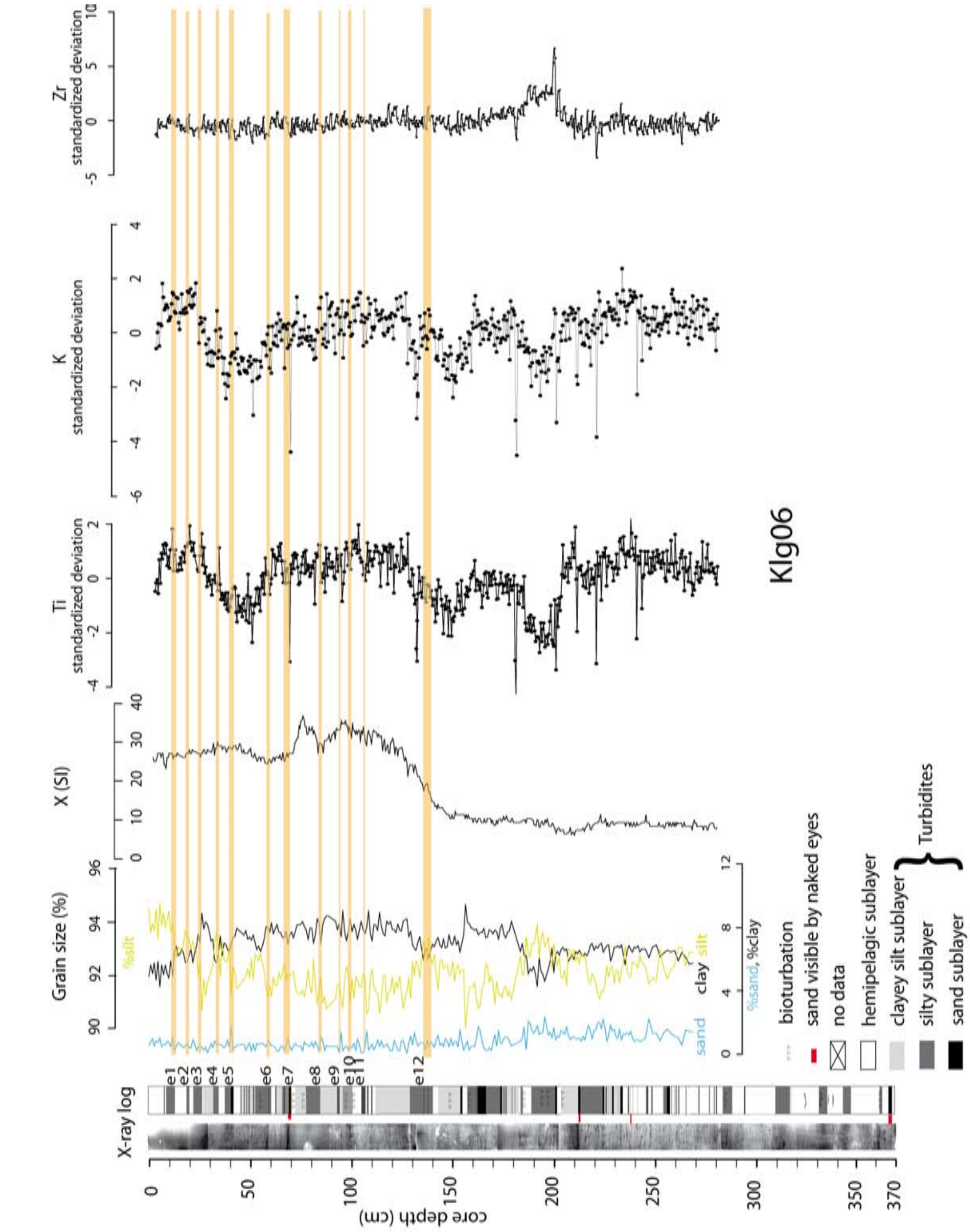

Figure 12: Stratigraphic log of the klg06 core situated in the Western High obtained combining X-ray imagery, grain size, magnetic susceptibility data, Mn and Zr standardized intensities. Main events deposited are identified and labelled.

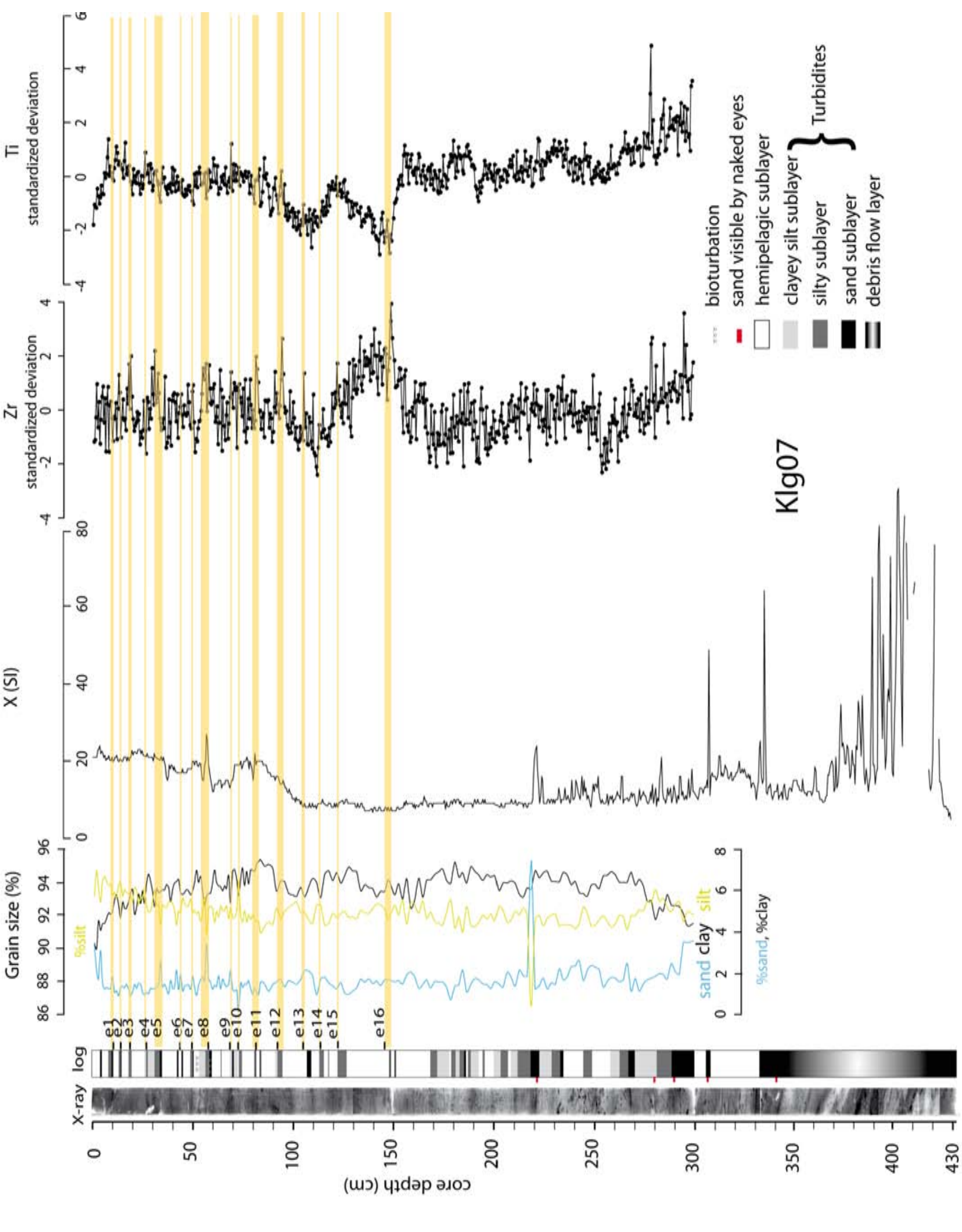

Figure 13: Stratigraphic log of the klg07 core situated in the Western High obtained combining X-ray imagery, grain size, magnetic susceptibility data, Mn and Zr standardized intensities. Main events deposited are identified and labelled; event label is changing according to their stratigraphic position, beginning with 1 at the top of the core.

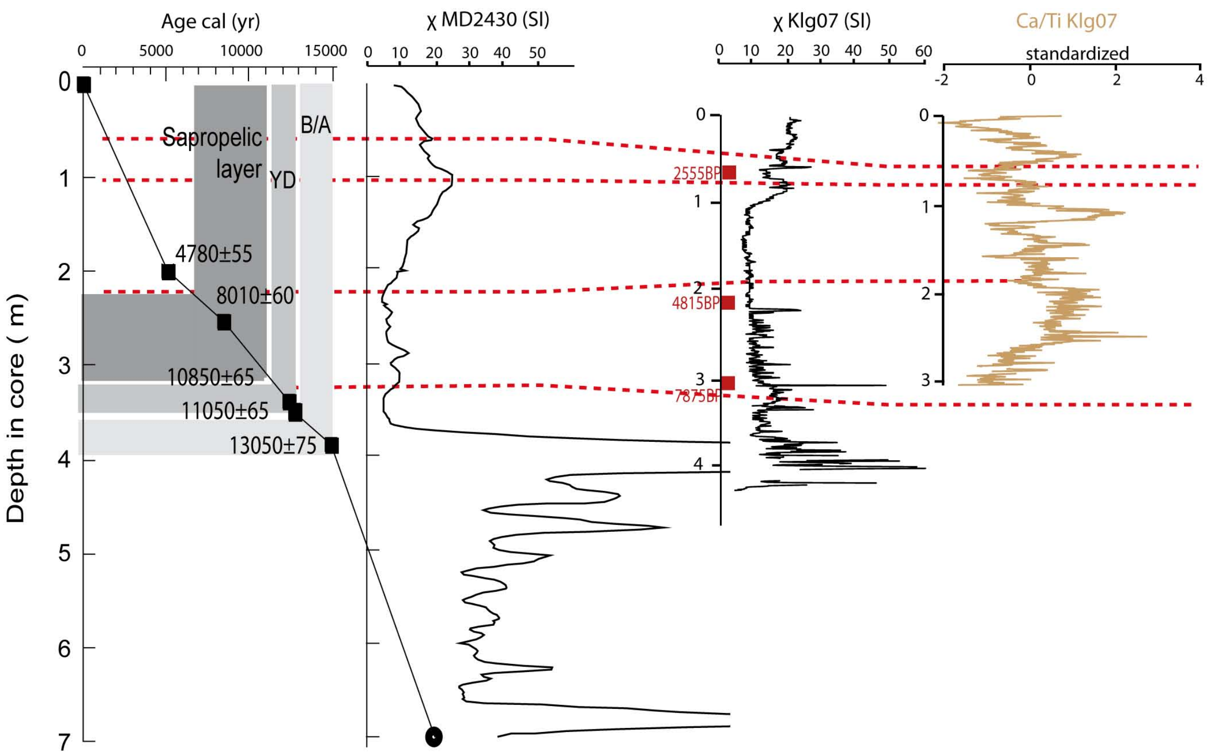

Figure 14: Core correlation between Klg07 and MD2430 (Vidal et al., 2010) in the Western High by using magnetic susceptibility data and Ca/Ti ratio. Red dashed line indicate key point of correlation. Uncalibrated ages are indicated in red and calibrated ones in black.

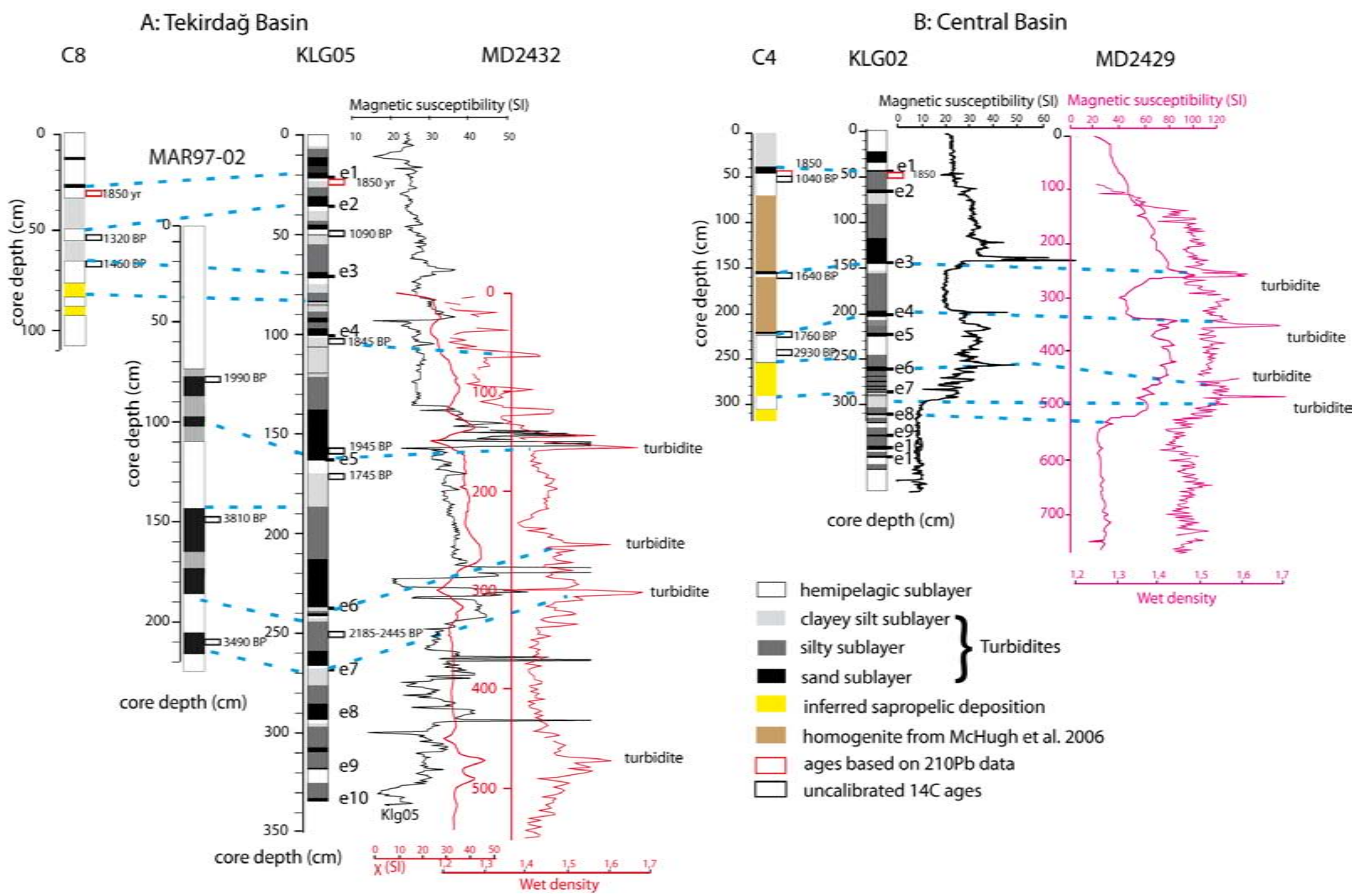

Figure 15: Core correlation between Klg02 and Klg05 and already publishe cores in the Central and Tekirdağ Basins. **A**: Correlation in the Tekirdağ Basin between the cores Klg05, MD2432, C8 (McHugh et al., 2006) and MAR97-02 (Hiscott et al., 2002) by using log and physical parameters. Uncalibrated ages are indicated for all the cores and key points of correlation are represented with blue dashed lines. **A**: Correlation in the CEntral Basin between the cores Klg02, MD2429 (Beck et al., 2007) and C4 (McHugh et al., 2006) by using log and physical parameters. Uncalibrated ages are indicated for all the cores and key points of correlation are represented with blue dashed lines.

References

Abrajano, T., Aksu, A., Hiscott, R., and Mudie, P.: Aspects of carbon isotope biogeochemistry of late Quaternary sediments from the Marmara Sea and Black Sea, Marine Geology, 190, 2002.

Adams, J.: Paleoseismicity of the Cascadia Subduction Zone - Evidence from Turbidites off the Oregon-Washington Margin, Tectonics, 9, 1990.

Aksoy, M., Meghraoui, M., Vallée, M., and Çakır, Z.: Rupture characteristics of the AD 1912 Mürefte (Ganos) earthquake segment of the North Anatolian fault (western Turkey), Geology, 38, 991, 2010.

Ambraseys, N.: The seismic activity of the Marmara Sea region over the last 2000 years, Bulletin of the Seismological Society of America, 92, 2002.

Armijo, R., Meyer, B., Hubert, A., and Barka, A.: Westward propagation of the North Anatolian fault into the northern Aegean: Timing and kinematics, Geology, 27, 267, 1999.

Armijo, R., Meyer, B., Navarro, S., King, G., and Barka, A.: Asymmetric slip partitioning in the Sea of Marmara pull-apart: a clue to propagation processes of the North Anatolian Fault?, Terra Nova, 14, 80–86, 2002.

Armijo, R., Pondard, N., Meyer, B., Uçarkuş, G., de Lepinay, B., Malavieille, J., Dominguez, S., Gutscher, M., Schmidt, S., Beck, C., Çağatay, N., Cakir, Z., Imren, C., Eriş, K., Natalin, B., Ozalaybey, S., Tolun, L., Lefevre, I., Seeber, L., Gasperini, L., Rangin, C., Emre, O., and Sarikavak, K.: Submarine fault scarps in the Sea of Marmara pull-apart (North Anatolian Fault): Implications for seismic hazard in Istanbul, Geochemistry Geophysics Geosystems, 6, 2005.

Bahr, A., Lamy, F., Arz, H., Kuhlmann, H., and Wefer, G.: Late glacial to Holocene climate and sedimentation history in the NW Black Sea, Marine Geology, 214, 309–322, 2005.

Barka, A. A. and Kadinsky-Cade, K.: Strike-slip fault geometry in Turkey and its influence on earthquake activity, Tectonics, 7, 663–684, 1988.

Bécel, A., Laigle, M., de Voogd, B., Hirn, A., Taymaz, T., Galvé, A., Shimamura, H., Murai, Y., Lépine, J., Sapin, M., et al.: Moho, crustal architecture and deep deformation under the North Marmara Trough, from the SEISMARMARA Leg 1 offshore-onshore reflection-refraction survey, Tectonophysics, 467, 1–21, 2009.

Beck, C., de Lépinay, B. M., Schneider, J., Cremer, M., Çağatay, N., Wendenbaum, E., Boutareaud, S., Ménot, G., Schmidt, S., Weber, O., Eris, K., Armijo, R., Meyer, B., Pondard, N., Gutscher, M., the Marmacore cruise party, Turon, J., Labeyrie, L., Cortijo, E., Gallet, Y., Bouquerel, H., Gorur, N., Gervais, A., Castera, M., Londeix, L., de Rességuier, A., and Jaouen, A.: Late Quaternary co-seismic sedimentation in the Sea of Marmara's deep basins, Sedimentary Geology, 199, 2007.

Bertrand, S., Charlet, F., Chapron, E., Fagel, N., and De Batist, M.: Reconstruction of the Holocene seismotectonic activity of the Southern Andes from seismites recorded in Lago Icalma, Chile, 39 S, Palaeogeography, Palaeoclimatology, Palaeoecology, 259, 301–322, 2008.

Bottema, S. and Woldring, H.: Bronze Age and Byzantine pollen of the Kestel tin-mine (Turkey) and its possible origin: practical and experimental pollen analysis in archaeological context, Aspects of archaeological palynology: methodology and applications. AASP Contributions Series, 29, 7–15, 1994.

Butler, R.: Paleomagnetism: magnetic domains to geologic terranes, Blackwell Scientific Publications Boston, MA, 1992.

Carton, H., Singh, S. C., Hirn, A., Bazin, S., de Voogd, B., Vigner, A., Ricolleau, A., Cetin, S., Ocakoglu, N., Karakoc, F., and Sevilgen, V.: Seismic imaging of the three-dimensional architecture of the Cinarcik Basin along the North Anatolian Fault, Journal of Geophysical Research-Solid Earth, 112, 2007.

Çağatay, M., Görür, N., Algan, O., Eastoe, C., Tchapalyga, A., Ongan, D., Kuhn, T., and Kuşcu, I.: Late Glacial-Holocene palaeoceanography of the Sea of Marmara: timing of connections with the Mediterranean and the Black Seas, Marine Geology, 167, 2000.

Dolan, J., Christofferson, S., and Shaw, J.: Recognition of paleoearthquakes on the Puente Hills blind thrust fault, California, Science, 300, 115, 2003.

Eastwood, W., Roberts, N., and Lamb, H.: Palaeoecological and archaeological evidence for human occupance in southwest Turkey: the Beyşehir occupation phase, Anatolian studies, 48, 69–86, 1998.

Eris, K. K., Ryan, W. B. F., Cagatay, M. N., Sancar, U., Lericolais, G., Menot, G., and Bard, E.: The timing and evolution of the post-glacial transgression across the Sea of Marmara shelf south of Istanbul, Marine Geology, 243, 2007.

Folk, R.: Petrology of sedimentary rocks, Hemphill's Austin, Texas, 1968.

Fraser, J., Vanneste, K., and Hubert-Ferrari, A.: Recent behavior of the North Anatolian Fault: Insights from an integrated paleoseismological data set, Journal of Geophysical Research, 115, 2010.

Galli, P., Galadini, F., and Pantosti, D.: Twenty years of paleoseismology in Italy, Earth-Science Reviews, 88, 89–117, 2008.

Goldfinger, C.: The Record of Large Turbidites and Their Relevance to the History of Earthquakes, Annual Review of Marine Science, 3, 2011.

Goldfinger, C., Nelson, C., and Johnson, J.: Holocene earthquake records from the Cascadia subduction zone and northern San Andreas fault based on precise dating of offshore turbidites, Annual Review of Earth and Planetary Sciences, 31, 555–577, 2003a.

Goldfinger, C., Nelson, C., Johnson, J. E., and the Shipboard Scientific party: Deep-water turbidites as Holocene earthquake proxies: the Cascadia subduction zone and Northern San Andreas Fault systems, Annals of Geophysics, 46, 2003b.

Goldfinger, C., Grijalva, K., Burgmann, R., Morey, A., Johnson, J., Nelson, C., Gutierrez-Pastor, J., Ericsson, A., Karabanov, E., Chaytor, J., et al.: Late Holocene rupture of the northern San Andreas fault and possible stress linkage to the Cascadia subduction zone, Bulletin of the Seismological Society of America, 98, 861, 2008.

Gorsline, D., De Diego, T., and Nava-Sanchez, E.: Seismically triggered turbidites in small margin basins: Alfonso Basin, Western Gulf of California and Santa Monica Basin, California Borderland, Sedimentary Geology, 135, 21–35, 2000.

Hiscott, R. and Aksu, A.: Late Quaternary history of the Marmara Sea and Black Sea from high-resolution seismic and gravity-core studies, Marine Geology, 190, 2002.

Hiscott, R., Aksu, A., Yasar, D., Kaminski, M., Mudie, P., Kostylev, V., MacDonald, J., Isler, F., and Lord, A.: Deltas south of the Bosphorus Strait record persistent Black Sea outflow to the Marmara Sea since similar to 10 ka, Marine Geology, 190, 2002.

Hubert-Ferrari, A., Barka, A., Jacques, E., Nalbant, S., Meyer, B., Armijo, R., Tapponnier, P., and King, G.: Seismic hazard in the Marmara Sea region following the 17 August 1999 Izmit earthquake, Nature, 404, 269–273, 2000.

Inouchi, Y., Kinugasa, Y., Kumon, F., Nakano, S., Yasumatsu, S., and Shiki, T.: Turbidites as records of intense palaeoearthquakes in Lake Biwa, Japan, Sedimentary Geology, 104, 117–125, 1996.

Kazanci, N., Leroy, S., Ileri, O., Emre, O., Kibar, M., and Oncel, S.: Late Holocene erosion in NW Anatolia from sediments of Lake Manyas, Lake Ulubat and the southern shelf of the Marmara Sea, Turkey, Catena, 57, 277–308, 2004.

Klinger, Y., Etchebes, M., Tapponnier, P., and Narteau, C.: Characteristic slip for five great earthquakes along the Fuyun fault in China, Nature Geoscience, 4, 389–392, 2011.

Kondo, H., Nakata, T., Akhtar, S., Wesnousky, S., Sugito, N., Kaneda, H., Tsutsumi, H., Khan, A., Khattak, W., and Kausar, A.: Long recurrence interval of faulting beyond the 2005 Kashmir earthquake around the northwestern margin of the Indo-Asian collision zone, Geology, 36, 731, 2008.

Le Pichon, X., Sengör, A., Demirbag, E., Rangin, C., Imren, C., Armijo, R., Görür, N., Çagatay, N., Mercier de Lepinay, B., Meyer, B., SaatçIlar, R., and Tok, B.: The active Main Marmara Fault, Earth and Planetary Science Letters, 192, 595 – 616, 2001.

Londeix, L., Herreyre, Y., Turon, J., and Fletcher, W.: Last Glacial to Holocene hydrology of the Marmara Sea inferred from a dinoflagellate cyst record, Review of Palaeobotany and Palynology, 158, 52–71, 2009.

Major, C., Ryan, W., Lericolais, G., and Hajdas, I.: Constraints on Black Sea outflow to the Sea of Marmara during the last glacial-interglacial transition, Marine Geology, 190, 19–34, 2002.

Masson, D., Arzola, R., Wynn, J., Hunt, E., and P., W.: Seismic triggering of landslides and turbidity currents offshore Portugal, Geochem. Geophys. Geosyst., 2011.

McClusky, S., Reilinger, R., Mahmoud, S., Ben Sari, D., and Tealeb, A.: GPS constraints on Africa (Nubia) and Arabia plate motions, Geophysical Journal International, 155, 126–138, 2003.

McHugh, C., Seeber, L., Braudy, N., Cormier, M., Davis, M., Diebold, J., Dieudonne, N., Douilly, R., Gulick, S., Hornbach, M., et al.: Offshore sedimentary effects of the 12 January 2010 Haiti earthquake, Geology, 39, 723, 2011.

McHugh, C. M. G., Seeber, L., Cormier, M.-H., Dutton, J., Cagatay, N., Polonia, A., Ryan, W. B. F., and Gorur, N.: Submarine earthquake geology along the North Anatolia Fault in the Marmara Sea, Turkey: A model for transform basin sedimentation, Earth and Planetary Science Letters, 248, 2006.

Migeon, S., Weber, O., Faugeres, J., and Saint-Paul, J.: SCOPIX: a new X-ray imaging system for core analysis, Geo-Marine Letters, 18, 251–255, 1999.

Mudie, P., Rochon, A., and Aksu, A.: Pollen stratigraphy of Late Quaternary cores from Marmara Sea: land-sea correlation and paleoclimatic history, Marine Geology, 190, 233–260, 2002.

Muller, J. and Aydin, A.: Using mechanical modeling to constrain fault geometries proposed for the northern Marmara Sea, Journal of Geophysical Research, 110, B03 407, 2005.

Nakajima, T. and Kanai, Y.: Sedimentary features of seismoturbidites triggered by the 1983 and older historical earthquakes in the eastern margin of the Japan Sea, Sedimentary Geology, 135, 1–19, 2000.

Örgülü, G.: Seismicity and source parameters for small-scale earthquakes along the splays of the North Anatolian Fault (NAF) in the Marmara Sea, Geophysical Journal International, 184, 2011.

Palike, H., Shackleton, N., and Rohl, U.: Astronomical forcing in Late Eocene marine sediments, Earth and Planetary Science Letters, 193, 589–602, 2001.

Pettijohn, F., Potter, P., and Siever, R.: Sand and sandstone, Springer, 1987.

Pondard, N.: Le pull-apart de la Mer de Marmara (Faille Nord Anatolienne): évolution morphologique et tectonique, interactions entre failles, et aléa sismique de la région d'Istanbul, Ph.D. thesis, Institut de Physique du Globe de Paris, 2006.

Pondard, N., Armijo, R., King, G. C. P., Meyer, B., and Flerit, F.: Fault interactions in the Sea of Marmara pull-apart (North Anatolian Fault): earthquake clustering and propagating earthquake sequences, Geophysical Journal International, 171, 2007.

Reilinger, R., McClusky, S., Vernant, P., Lawrence, S., Ergintav, S., Cakmak, R., Ozener, H., Kadirov, F., Guliev, I., Stepanyan, R., et al.: GPS constraints on continental deformation in the Africa-Arabia-Eurasia continental collision zone and implications for the dynamics of plate interactions, Journal of Geophysical Research, 111, B05 411, 2006.

Robbins, J.: Geochemical and geophysical applications of radioactive lead, The biogeochemistry of lead in the environment, 1, 285–337, 1978.

Rockwell, T., Ragona, D., Seitz, G., Langridge, R., Aksoy, M., Uçarkuş, G., Ferry, M., Meltzner, A., Klinger, Y., Meghraoui, M., et al.: Palaeoseismology of the North Anatolian Fault near the Marmara Sea: implications for fault segmentation and seismic hazard, Geological Society, London, Special Publications, 316, 31, 2009.

Sarı, E. and Çağatay, M.: Turbidites and their association with past earthquakes in the deep Çınarcık Basin of the Marmara Sea, Geo-Marine Letters, 26, 2006.

Schmidt, S., Howa, H., Mouret, A., Lombard, F., Anschutz, P., and Labeyrie, L.: Particle fluxes and recent sediment accumulation on the Aquitanian margin of Bay of Biscay, Continental Shelf Research, 29, 1044–1052, 2009.

Seeber, L., Cormier, M., McHugh, C., Emre, O., Polonia, A., and Sorlien, C.: Rapid subsidence and sedimentation from oblique slip near a bend on the North Anatolian transform fault in the Marmara Sea, Turkey, Geology, 34, 933, 2006.

Seeber, L., Emre, O., Cormier, M., Sorlien, C., McHugh, C., Polonia, A., Ozer, N., and Çağatay, N.: Uplift and subsidence from oblique slip: the Ganos-Marmara bend of the North Anatolian Transform, Western Turkey, Tectonophysics, 391, 2004.

Sengör, A., Tüysüz, O., Imren, C., Sakinç, M., Eyidogan, H., Görür, N., Le Pichon, X., and Rangin, C.: The North Anatolian fault: A new look, Annu. Rev. Earth Planet. Sci., 33, 37–112, 2005.

Shiki, T., Kumon, F., Inouchi, Y., Kontani, Y., Sakamoto, T., Tateishi, M., Matsubara, H., and Fukuyama, K.: Sedimentary features of the seismo-turbidites, Lake Biwa, Japan, Sedimentary Geology, 135, 37–50, 2000.

Sperazza, M., Moore, J., and Hendrix, M.: High-resolution particle size analysis of naturally occurring very fine-grained sediment through laser diffractometry, Journal of Sedimentary Research, 74, 736, 2004.

Tauxe, L.: Essentials of Paleomagnetism, University of California Press, 2010.

Uçarkuş, G.: Active faulting and earthquake scarps along the North Anatolian Fault in the Seo of Marmara., Ph.D. thesis, Istanbul Technical University, 2010.

Van Zeist, W., Woldring, H., and Stapert, D.: Late Quaternary vegetation and climate of southwestern Turkey, Palaeohistoria, 17, 53–143, 1975.

Vidal, L., Menot, G., Joly, C., Bruneton, H., Rostek, F., Çağatay, M. N., Major, C., and Bard, E.: Hydrology in the Sea of Marmara during the last 23 ka: Implications for timing of Black Sea connections and sapropel deposition, Paleoceanography, 25, 2010.

Vlag, P. A., Kruiver, P. P., and Dekkers, M. J.: Evaluating climate change by multivariate statistical techniques on magnetic and chemical properties of marine sediments (Azores region), Palaeogeography, Palaeoclimatology, Palaeoecology, 212, 23 – 44, 2004.

Weldon, R., Scharer, K., Fumal, T., and Biasi, G.: Wrightwood and the earthquake cycle: what a long recurrence record tells us about how faults work, GSA TODAY, 14, 4–10, 2004.